

1 **Experimental application of FRF-based model updating approach to estimate soil mass and**
2 **stiffness mobilised under pile impact tests**

3 Prendergast, L.J.^{a,1}, Wu, W.H.^{b,2}, Gavin, K.^{c,3}

4 ^a Department of Civil Engineering,
5 Faculty of Engineering,
6 University of Nottingham,
7 Nottingham,
8 NG7 2RD,
9 United Kingdom

10
11 ^b Department of Construction Engineering,
12 National Yunlin University of Science and Technology,
13 Section 3, Daxue Road,
14 Douliu City,
15 Yunlin 640,
16 Taiwan

17
18 ^c Faculty of Civil Engineering and Geosciences,
19 Delft University of Technology,
20 Building 23,
21 Stevinweg 1 / PO-box 5048,
22 2628 CN Delft / 2600 GA Delft,
23 The Netherlands

24
25 ¹Corresponding author

26
27 Email: 1luke.prendergast@nottingham.ac.uk, 2wuwh@yuntech.edu.tw, 3k.g.gavin@tudelft.nl

28
29 **Abstract**

30 The dynamic response of structures in contact with soil is receiving increasing interest and there is a
31 growing need for more accurate models capable of simulating the behaviour of these systems. This is
32 particularly important in the field of offshore wind turbines, where accurate estimates of system
33 frequency are needed to avoid resonance, and in the structural health monitoring fields, where
34 accurate reference damage models are used. Previous work has shown that there is significant
35 uncertainty in how to specify mobilised soil stiffness for dynamic soil-pile interaction modelling.
36 Moreover, the contribution of soil mass in dynamic motion is often ignored. This paper applies a
37 finite-element iterative model updating approach previously developed by the authors to two
38 experimental piles to ascertain the mobilised soil stiffness and mass profiles from impact test data.
39 The method works by obtaining a frequency response function (FRF) from an impact test performed
40 on a test pile, developing a numerical model of this system, applying initial estimates of soil mass and
41 stiffness, and updating these properties to match the experimental FRF with that generated in the
42 numerical model. A range of elements are investigated including multiple runs of the approach to test

43 repeatability, the influence of different starting estimates for stiffness, the effect of variability in
44 experimental test data, and the influence of the pile length over which masses are distributed.
45 Moreover, potential sources of error are discussed. The method provides reasonably consistent
46 estimates of the soil stiffness and mass acting in the lateral dynamic motion of a given pile tested in
47 this paper. The approach may be useful in the continued improvement of Soil-Structure Interaction
48 (SSI) modelling for dynamic applications.

49 **Keywords:** Soil Stiffness; Model-Updating; Dynamics; Mass; Winkler; Soil-Structure Interaction

50

51 1. Introduction

52 There is increasing interest in the dynamic response of structures incorporating soil-structure
53 interaction, particularly in the fields of Earthquake [1,2] and Offshore Engineering [3–6] among
54 others. For offshore wind turbines, accurate knowledge of the soil-structure interaction behaviour is
55 paramount to the safe operation of these structures due to the potential for resonance from waves and
56 the spinning rotor, which can exacerbate fatigue. In recent times, the field of vibration-based
57 Structural Health Monitoring (SHM), which traditionally focussed on detecting damage in super-
58 structural components such as bridge beams [7–9], has begun to focus on damage detection of
59 foundations [10–14]. These recent developments have led to an urgency relating to the need for
60 accurate models capable of encapsulating the behaviour of soil-structure interaction systems.

61 The development of numerical models for structural simulations has been the recourse for design
62 engineers for many years, since it is not possible to experimentally trial every load-case a structure
63 may incur. It is unusual for a developed numerical model of a given structural system to perfectly
64 model the behaviour at the first trial, therefore the field of Finite-Element (FE) model updating has
65 focussed on utilising information from the actual structural response to modify the parameters of the
66 numerical model in order to minimise the differences in behaviour between the model and the real
67 system. This is particularly important in the field of structural damage detection where reference
68 numerical models of assets such as bridges are required to benchmark normal operating behaviour. In
69 dynamic modelling fields, model updating approaches have received much attention in recent years
70 [15–23]. Imregun et al. [15] developed a Frequency Response Function (FRF)-based model updating
71 approach and investigated its performance against several barriers for implementation including noisy
72 experimental data and the uniqueness of the updated model when applied to the case of a beam.
73 Experimental noise posed an issue to the accuracy of the method. Nalitolela et al. [16] demonstrated a
74 FRF-based approach using experimental and simulated data, which was based on the addition of
75 artificial stiffness to the structure. A sensitivity procedure was used to update the model parameters.
76 Esfandiari et al. [20] developed a model updating approach to identify the presence of damage by

77 updating the stiffness and mass of the structure using a FRF-based method applied to a truss model. A
78 similar study by Hwang and Kim [18] focussed on estimating damage severity and location using
79 FRFs for a cantilever beam and a helicopter rotor blade model. Wu et al. [23] presented a FRF-based
80 approach to estimate the mass and stiffness of soil contributing to the lateral dynamic motion of
81 simulated foundation piles, and demonstrated the method using numerically simulated data for typical
82 pile geometries and soil spring stiffness.

83 This paper is an advancement on work presented by Prendergast and Gavin [6] and Wu et al. [23].
84 Prendergast and Gavin [6] investigated the variation in modelled dynamic response of soil-pile
85 systems through the implementation of different formulations of soil spring stiffness. The various
86 formulations, termed coefficients of subgrade reaction (in static case), require the specification of pile
87 structural and geometric parameters such as Young's modulus (E), second moment of area (I), pile
88 diameter (D) and soil properties including small-strain stiffness (E_0) and Poisson's ratio (ν_s). These
89 expressions, originally derived for static applications under specified operational strain, led to
90 significantly varied dynamic responses in the study conducted in [6], both in predicted acceleration
91 magnitude and frequency. This study highlighted the significant uncertainty that persists in the
92 selection of an appropriate subgrade reaction model to transform identical soil and pile properties, as
93 significantly different responses were predicted. The present study applies the FRF-based model
94 updating approach developed by Wu et al. [23] to the experimental case study data of two piles in [6],
95 with a view to estimating the soil mass and stiffness mobilised in the dynamic motion. The FRF of a
96 given pile is derived using the input force time-history and the output acceleration-time history from
97 experimental testing, and this is used as the target in the updating method. A numerical beam-Winkler
98 model is developed with an initial soil stiffness profile, estimated using a variety of subgrade reaction
99 formulations and available geotechnical data [6]. This stiffness is applied in the numerical model and
100 the soil mass is initially guessed. The method then updates the stiffness and mass at the soil-structure
101 interface in the beam-Winkler model until the experimental FRF and the numerical FRF generated in
102 the model match within a defined tolerance. The approach aims to reduce the uncertainty in the
103 selection of a soil stiffness profile by enabling a simple model updating approach using a single FRF
104 from the target structure.

105

106 **2. Numerical modelling of piles**

107 In this section, the methods adopted to formulate numerical FE models of piles to model their
108 dynamic responses are described.

109

110 **2.1 Mathematical formulation**

111 Numerical beam-Winkler models are developed to simulate the behaviour of real test piles, described
 112 in Section 4. A FE model from which to obtain the dynamic response of a pile to a lateral impact is
 113 modelled in this paper using Euler-Bernoulli beam elements [24] to model the pile, and Winkler
 114 spring elements [25,26] to model the soil. Soil mass is incorporated by adding lumped masses to the
 115 nodes connecting Winkler spring elements to the pile elements. The global dynamic response is
 116 governed by Eq. (1).

$$117 \quad \mathbf{M}_G \{\ddot{\mathbf{x}}(t)\} + \mathbf{C}_G \{\dot{\mathbf{x}}(t)\} + \mathbf{K}_G \{\mathbf{x}(t)\} = \{\mathbf{P}(t)\} \quad (1a)$$

118 where \mathbf{M}_G , \mathbf{C}_G and \mathbf{K}_G are the $(N \times N)$ global mass, damping and stiffness matrices for the pile-soil
 119 system; N is the total number of degrees of freedom (DOF) and

$$120 \quad \mathbf{x}(t) = \{x_1(t) \quad x_2(t) \quad \dots \quad x_N(t)\}^T \quad (1b)$$

$$121 \quad \dot{\mathbf{x}}(t) = \{\dot{x}_1(t) \quad \dot{x}_2(t) \quad \dots \quad \dot{x}_N(t)\}^T \quad (1c)$$

$$122 \quad \ddot{\mathbf{x}}(t) = \{\ddot{x}_1(t) \quad \ddot{x}_2(t) \quad \dots \quad \ddot{x}_N(t)\}^T \quad (1d)$$

$$123 \quad \mathbf{P}(t) = \{P_1(t) \quad P_2(t) \quad \dots \quad P_N(t)\}^T \quad (1e)$$

124 where $\mathbf{x}(t)$, $\dot{\mathbf{x}}(t)$ and $\ddot{\mathbf{x}}(t)$ are the displacement, velocity and acceleration of each DOF in the model,
 125 for each time step. Damping is modelled using Cauchy damping, employing a two-term Rayleigh
 126 formulation [27]. The damping ratio used is measured from the experimental signals, see Section 4.
 127 The dynamic response is obtained by solving Eq. (1) using the Wilson- θ integration scheme [28,29].
 128 The natural frequencies and mode shapes of the soil-pile system may be calculated by solving the
 129 Eigenproblem [27] of the system matrix $\mathbf{D}_{\text{SYS}} = \mathbf{M}_G^{-1}\mathbf{K}_G$. Further details on the numerical modelling
 130 employed are available in Wu et al. [23]. In this paper, the mass and stiffness matrices for the pile
 131 model are derived using the material and geometrical properties of the test piles, described in Section
 132 4. The force vector $\mathbf{P}(t)$ is populated using the force time-history from a modal hammer impact,
 133 described in Section 4.

134 **2.2 Soil stiffness using subgrade reaction approach**

135 The present paper is an evolution of work presented by Prendergast and Gavin [6] which assessed the
 136 performance of five particular formulations of subgrade reaction in modelling the small-strain
 137 dynamic response of laterally vibrating piles. These models were developed by Biot [30], see Eq. (2),

138 Vesic [31,32], see Eq. (3), Meyerhof and Baice [33,34], see Eq. (4), Klopple and Glock [33–35], see
 139 Eq. (5) and Selvadurai [34,35], see Eq. (6). The research in [6] concluded that for the given field
 140 conditions and pile parameters considered, the Vesic model (Eq. 3) provided the closest
 141 approximation to the frequency response of two experimental piles, with deviations of 16.6% and
 142 3.9% respectively. However, the analysis highlighted the significant disparity in predicted response
 143 depending on which formulation was implemented, and moreover the analysis assumed no soil mass
 144 contributed to the dynamic behaviour of the pile-soil system. In this paper, these subgrade reaction
 145 models are used to specify the initial stiffness guess in the model-updating approach.

$$146 \quad k_s = \frac{0.95E_0}{D(1-\nu_s^2)} \left[\frac{E_0 D^4}{(1-\nu_s^2)EI} \right]^{0.108} \quad (2)$$

$$147 \quad k_s = \frac{0.65E_0}{D(1-\nu_s^2)} \left[\frac{E_0 D^4}{EI} \right]^{1/12} \quad (3)$$

$$148 \quad k_s = \frac{E_0}{D(1-\nu_s^2)} \quad (4)$$

$$149 \quad k_s = \frac{2E_0}{D(1+\nu_s)} \quad (5)$$

$$150 \quad k_s = \frac{0.65}{D} \frac{E_0}{(1-\nu_s^2)} \quad (6)$$

151 where E_0 is the small-strain Young's modulus of soil (N/m²), D is the pile diameter (m), ν_s is the
 152 Poisson ratio, E is the Young's modulus of the pile material (N/m²) and I is the cross-sectional
 153 moment of inertia (m⁴). The E_0 profile for a given site can be estimated using shear wave velocity
 154 measurements [36,37], or from correlations to other geotechnical site investigation tests such as Cone
 155 Penetration Test (CPT) data [3,38–40]. The method for converting the moduli of subgrade reaction to
 156 individual spring moduli is detailed in Prendergast et al. [13].

157

158 **3 Soil mass and stiffness iterative updating method**

159 A graphical representation of the model updating approach developed by Wu et al. [23] to estimate
 160 the soil mass and stiffness acting along a pile is shown in Fig. 1 and an overview of the procedure is
 161 summarised herein.

162 An experimental FRF is obtained from an impact test on the pile for which the soil stiffness and mass
163 are sought, using Eq.(7) [6,41,42].

$$164 \quad H_a(\bar{\omega}) = \frac{\ddot{X}(\bar{\omega})}{P(\bar{\omega})} \quad (7)$$

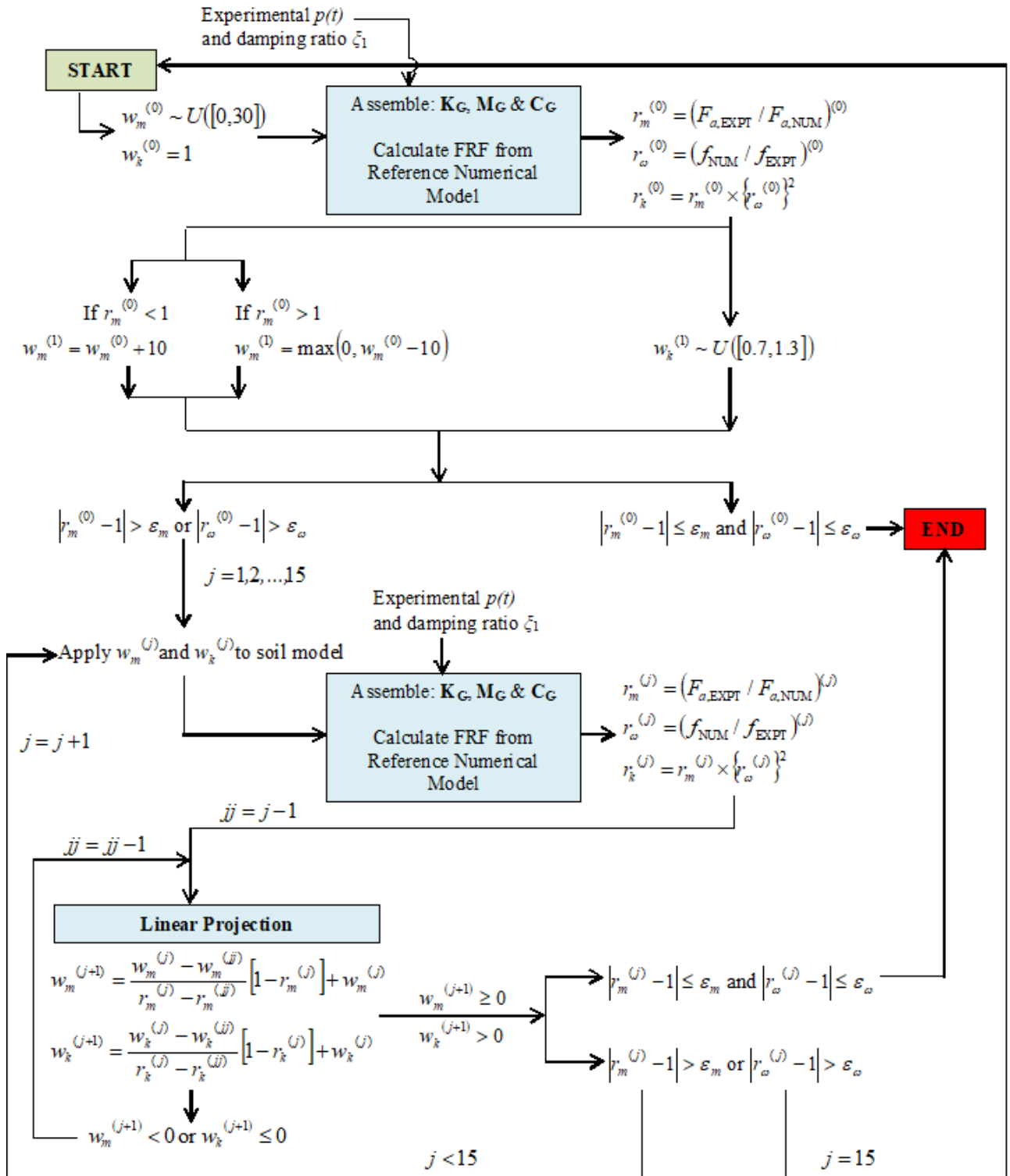
165 where $P(\bar{\omega})$ is the Fourier transform of the input force time-history $p(t)$ from a modal hammer and
166 $\ddot{X}(\bar{\omega})$ is the Fourier transform of the output acceleration time-history $\ddot{x}(t)$ from an accelerometer.
167 The amplitude of the complex-valued FRF in Eq. (7) is denoted by $F_a(\bar{\omega}) = |H_a(\bar{\omega})|$. It is assumed
168 that the material and geometry of this pile are known to the user so that a *reference* beam-Winkler
169 numerical model of the system can be created using the approach in Section 2.1. Using site
170 investigation data such as shear wave measurements and employing a subgrade reaction model such
171 as in Eqs. (2)-(6), soil spring stiffnesses can be applied in the numerical model as the initial *educated*
172 *guess* as to the acting soil stiffness in the system. A stiffness weighting, w_k is initially assumed as 1
173 times this profile. An initial guess of soil mass is postulated from a uniform distribution of mass
174 weightings, w_m between 0 and 30, to be multiplied by the known pile mass, m_p and distributed among
175 the sprung pile nodes in the reference numerical model. The information is used to assemble mass,
176 \mathbf{M}_G and stiffness, \mathbf{K}_G matrices using the approach in Section 2.1. The numerical model also requires
177 an estimate of the damping of the real system and, as a Rayleigh formulation is adopted in the
178 modelling, the damping ratio of the first mode ζ_1 is required. This can be estimated from the
179 experimental time-domain response using the logarithmic decrement technique [43] or through fitting
180 exponential decay functions [44]. This can also be estimated in the frequency domain using the half-
181 power bandwidth method [43]. The damping matrix \mathbf{C}_G is then formulated as a linear combination of
182 \mathbf{M}_G and \mathbf{K}_G , using this specified damping ratio [27]. Once a numerical model employing an initial
183 guess of the soil properties of the real system is developed, one can generate a first estimate numerical
184 FRF by applying the force time-history from the experimental test to a node in the numerical model
185 close to the point of application on the real system, and the acceleration response of the system may
186 be calculated by solving Eq. (1). The output acceleration from the node closest to the accelerometer
187 on the real system is used in the FRF specification. After the first run of the numerical model, one
188 now has a FRF from the experimental test, and a FRF from the numerical model. A mass ratio is
189 defined as $r_m = F_{a,EXPT} / F_{a,NUM}$ where $F_{a,EXPT}$ is the peak amplitude of the experimental acceleration
190 FRF and $F_{a,NUM}$ is the peak amplitude of the calculated numerical FRF. A frequency ratio is defined as
191 $r_\omega = f_{NUM} / f_{EXPT}$ where f_{NUM} is the frequency associated with $F_{a,NUM}$ and f_{EXPT} is the frequency
192 associated with $F_{a,EXPT}$. The peak information (amplitude and frequency) from both FRFs can be used
193 to obtain r_m , r_ω and subsequently to calculate $r_k = r_m \times (r_\omega)^2$. These values are stored for use later in

194 the linear projection. Two convergence criteria are defined; ε_ω is the frequency convergence
 195 tolerance and ε_m is mass convergence tolerance. For all experimental trials in this paper, the
 196 convergence criteria are set to 1%.

197 For the second run of the iterative method, the soil mass estimate is either increased or decreased
 198 depending on the magnitude of r_m from the initial run. If $r_m^{(0)} < 1$, the mass should increase as this was
 199 underestimated in the numerical model in the first run. If $r_m^{(0)} > 1$, the mass weighting should
 200 decrease. The mass weighting is increased or decreased by an arbitrary value of 10 for the second
 201 guess, with a minimum mass of zero applied (no negative mass). The value '10' is not important, as
 202 the actual mass weighting is calculated in later iterations using the two starting estimates from
 203 iteration⁽⁰⁾ and iteration⁽¹⁾. For the stiffness weighting, the second guess is chosen from a uniform
 204 distribution of values between 0.7 and 1.3, to be multiplied by the initial soil stiffness profile. Once
 205 again, the actual value is unimportant, as two starting estimates are required in the iterative approach
 206 to allow the system minimise the difference in the FRF peak information and converge on mobilised
 207 weightings to be applied to the stiffness and mass estimates. Once the second run stiffness and mass
 208 weightings are specified (and stored), the system checks if the results of the initial first run are within
 209 the defined tolerance, i.e. less than 1% difference in FRF peak amplitudes and frequencies between
 210 experimental and numerical FRFs. If they are not, the second guess weightings are applied to the
 211 profiles in the numerical model. New \mathbf{M}_G , \mathbf{K}_G and \mathbf{C}_G matrices are assembled, the force time-history
 212 is applied, the output acceleration is calculated, and a new FRF is generated. There now exists two
 213 estimates of the FRF of the system, iteration⁽⁰⁾ and iteration⁽¹⁾. Both of these estimates are used to
 214 initiate the linear projection method to calculate further weightings for stiffness and mass towards
 215 convergence. These further weightings are updated using the mass ratio, r_m , and the frequency ratio,
 216 r_ω , from the current and previous iterations, and the stiffness ratio defined by $r_k = r_m \times (r_\omega)^2$. The
 217 linear projection aims to minimise the difference in FRF peak value and frequency between the
 218 generated numerical FRF and the target experimental FRF. Once the calculated weightings lead to the
 219 generation of a numerical FRF that converges on the experimental FRF, the method terminates and
 220 outputs the converged soil stiffness profile and added soil mass.

221 Due to the tendency for error propagation in automated optimisation processes, some inadmissibility
 222 checks and boundary conditions are implemented in the procedure. It is possible for the linear
 223 projection method to postulate a negative weighting for stiffness or mass. If this happens, the linear
 224 projection method automatically re-calculates the new weighting using the j^{th} and $(j-2)^{\text{th}}$, j^{th} and $(j-3)^{\text{th}}$... j^{th} and $(j-i)^{\text{th}}$ iterations until admissible weightings are produced. Should the $(j-i)^{\text{th}}$ iteration reach
 225 the first iteration of the method without an admissible weighting being obtained, the new weighting is
 226 calculated by multiplying the value of the j^{th} iteration by a random value between 0.9 and 1.1 (i.e. the
 227

228 current weighting is varied by $\pm 10\%$), then the method continues as normal. Additionally, if
 229 convergence is not achieved within (an arbitrary) 15 iterations, the system resets and re-initialises all
 230 of the parameters.



231

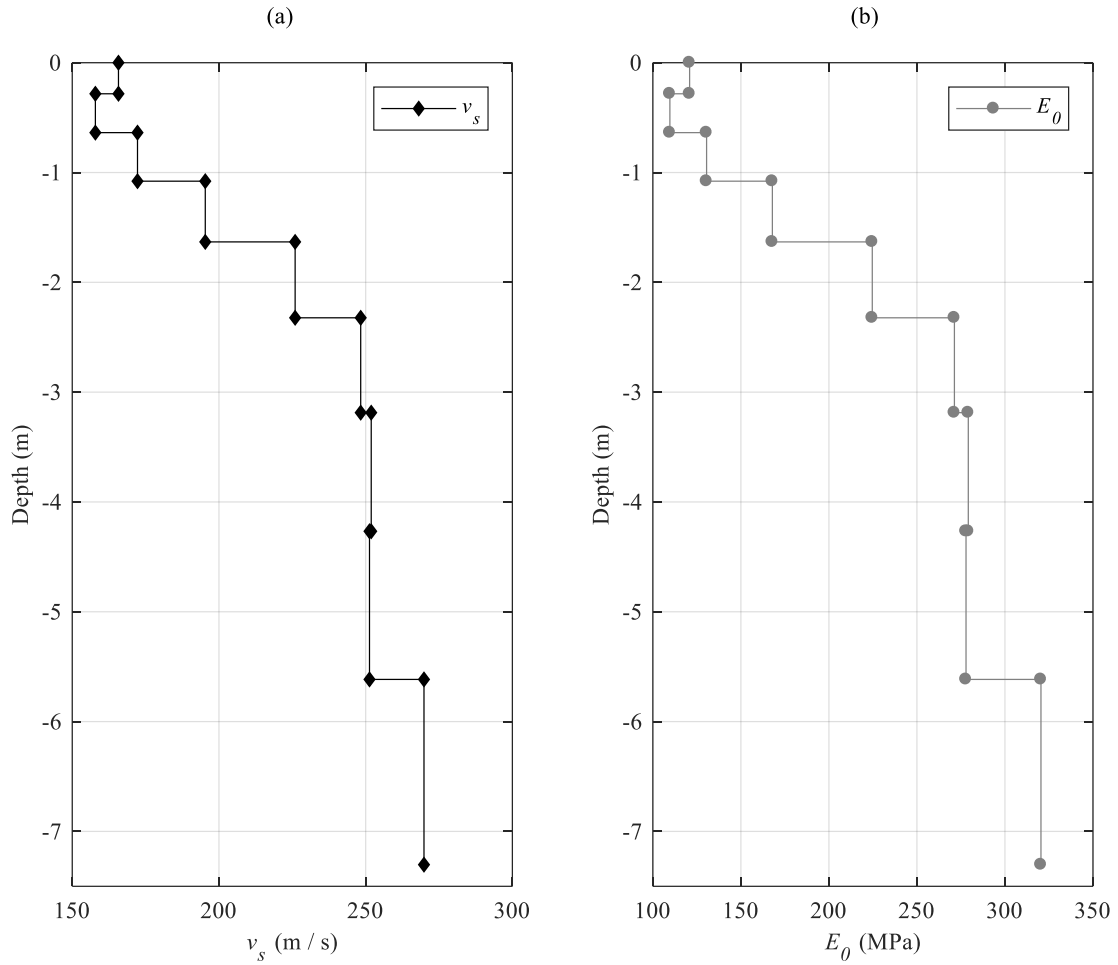
232

Fig. 1. Flow chart of iterative algorithm

233 4 Experimental pile tests

234 Data from a field test conducted in Prendergast and Gavin [6] is used to test the iterative updating
235 approach developed in Wu et al. [23]. A summary of the field test and information relating to the new
236 analysis is described herein. Lateral vibration tests were conducted on two 0.34 m diameter open-
237 ended steel piles driven into dense, over-consolidated sand at a quarry in Blessington, southwest of
238 Dublin, Ireland. Prior to testing, both piles were excavated by different amounts to give L/D ratios of
239 13 and 9 for Pile 1 and 2, respectively, see Fig. 6(a).

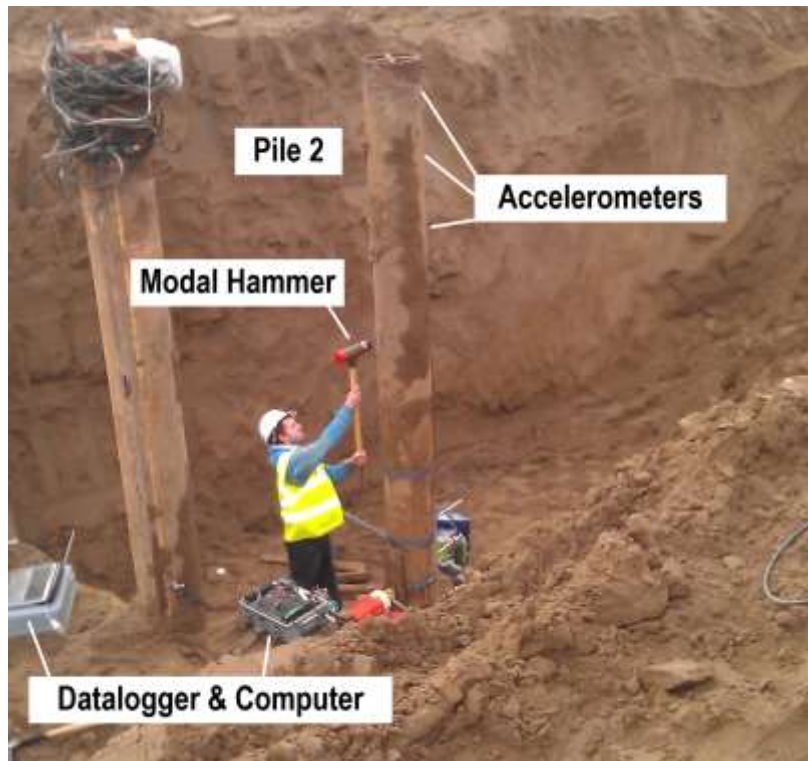
240 The test quarry has been characterised in detail [45] and used to investigate the performance of a
241 number of model, prototype and full scale foundation concepts over the last number of years [46–49].
242 A full description of the geotechnical properties of the site can be obtained in [37,45,46,50]. The
243 small-strain stiffness properties of the site, measured using Multi-Channel Analysis of Surface Waves
244 (MASW), see [36], are required for the approach in this paper. The shear wave velocity profile, Fig.
245 2(a) is used to derive the small-strain Young's modulus profile, Fig. 2(b) by first calculating the
246 small-strain shear modulus (G_0) using $G_0 = \rho v_s^2$ and $E_0 = 2G_0(1 + \nu)$, where ρ is the soil density
247 (kg/m^3) and ν is the small-strain Poisson ratio, taken as 0.1.



248

249 Fig. 2. Small-strain soil stiffness data. (a) shear wave velocity measurements, (b) derived E_0 profile.

250



251

252

Fig. 3. Photo of impact testing on Pile 2

253 Each pile was fitted with three accelerometers distributed along the exposed portion of the pile shaft,
 254 see Fig. 6(a), and these accelerometers were programmed to scan at 1000Hz. Note, only the top
 255 accelerometer is used in the procedure while the remaining two accelerometers are used to ensure
 256 consistency in the data. The test procedure (for a given pile) involved impacting the pile laterally with
 257 a PCB Piezotronics 086D50 model sledgehammer-type modal hammer [51](tip mass = 5.5 kg) and
 258 measuring the resulting acceleration signal from the accelerometers, see Fig. 3. A number of hammer
 259 impacts were undertaken on each pile to investigate repeatability. Each acceleration signal was low-
 260 pass filtered with a cut-off at 60 Hz to reduce the contribution of higher modes and noise, and a FRF
 261 is then generated, which is used as the target data in the numerical analysis to estimate the stiffness
 262 and mass contribution of the soil.

263 The damping ratio is estimated for each impact test by fitting an exponential curve to the peaks of the
 264 filtered acceleration signal in the time-domain, see [6,44], and validated using a logarithmic
 265 decrement technique [43].

266 FRFs of velocity and displacement are derived from the acceleration FRF using Eqs. (8) and (9).
 267 These FRFs are used to test the convergence of the iterative approach in the sense that if the
 268 converged soil mass and stiffness estimates provide a match in F_a , F_v and F_d , this acts as an additional
 269 check to mitigate false positives. Note, F_v and F_d are not used directly in the iterative updating

270 approach (see Fig. 1), but only used as a check in the converged model. Note also that these are
 271 derived from F_a because the pile velocity and displacement are not measured in the experiment.

$$272 \quad F_v(\bar{\omega}) = \left| \frac{H_a(\bar{\omega})}{i\bar{\omega}} \right| = \frac{F_a(\bar{\omega})}{\bar{\omega}} \quad (8)$$

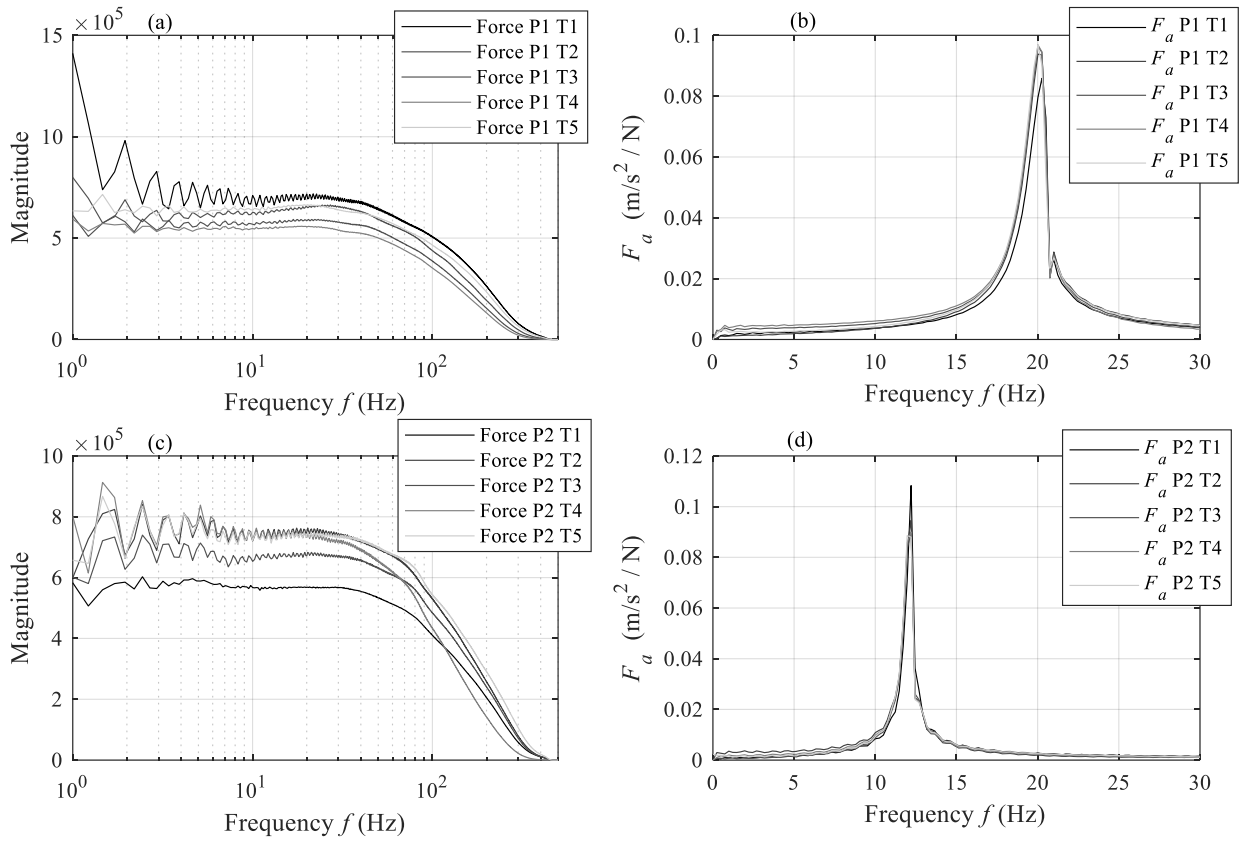
$$273 \quad F_d(\bar{\omega}) = \left| \frac{H_a(\bar{\omega})}{(i\bar{\omega})^2} \right| = \frac{F_a(\bar{\omega})}{\bar{\omega}^2} \quad (9)$$

274 where $\bar{\omega}$ is the variable of excitation. The FRFs for five impact tests conducted on Pile 1 and 2
 275 respectively are shown in Fig. 4 and the data is presented in Table 1. Damping data specified is from
 276 the curve fitting approach. Fig. 4(a) shows the frequency content of the force time-histories for the
 277 five impacts applied to Pile 1. Fig. 4(b) shows the acceleration FRFs for these five impacts on Pile 1.
 278 Fig. 4(c) shows the frequency content of the force time-histories for the five impacts applied to Pile 2.
 279 Fig. 4(d) shows the acceleration FRFs for these five impacts on Pile 2. The frequency content of the
 280 force-time histories is relatively uniform in the range of interest in this paper.

281 Table 1 Experimental data

Test	Frequency (Hz)	Damping ratio (%) – curve fitting method
P1 T1	20.26	1.77
P1 T2	20.02	1.72
P1 T3	20.02	1.85
P1 T4	20.02	1.77
P1 T5	20.02	1.93
P2 T1	12.21	1.07
P2 T2	12.21	1.24
P2 T3	12.21	1.30
P2 T4	12.21	1.33
P2 T5	12.21	1.30

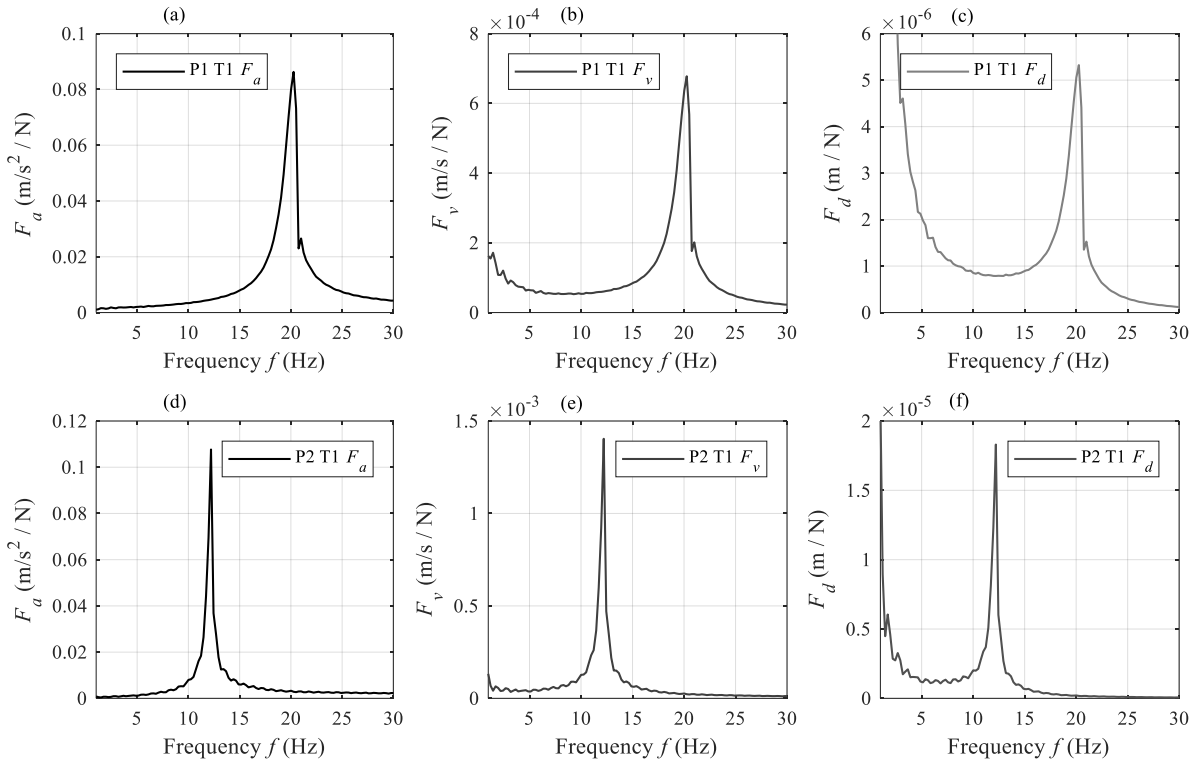
282 *P1 = Pile 1, P2 = Pile 2, T = Test No.



283

284 Fig. 4. Pile impact test data. (a) Frequency content of force time-history for five impact tests T1-T5 on
 285 Pile 1, (b) FRF from each impact test on Pile 1, (c) Frequency content of force time-history for five
 286 impact tests T1-T5 on Pile 2, (d) FRF from each impact test on Pile 2.

287 Using Eqs. (8) and (9), F_a can be converted to F_v and F_d . Fig. 5 shows the derived F_v and F_d from the
 288 first impact test conducted on both Pile 1 and Pile 2. These are used as a means to check the
 289 converged mass and stiffness weightings at the end of applying the method.



290

291 Fig. 5. Frequency Response Functions for the first impact test conducted on Pile 1 and 2. (a) Pile 1 F_a ,
 292 (b) Pile 1 F_v , (c) Pile 1 F_d , (d) Pile 2 F_a , (e) Pile 2 F_v , (f) Pile 2 F_d .

293

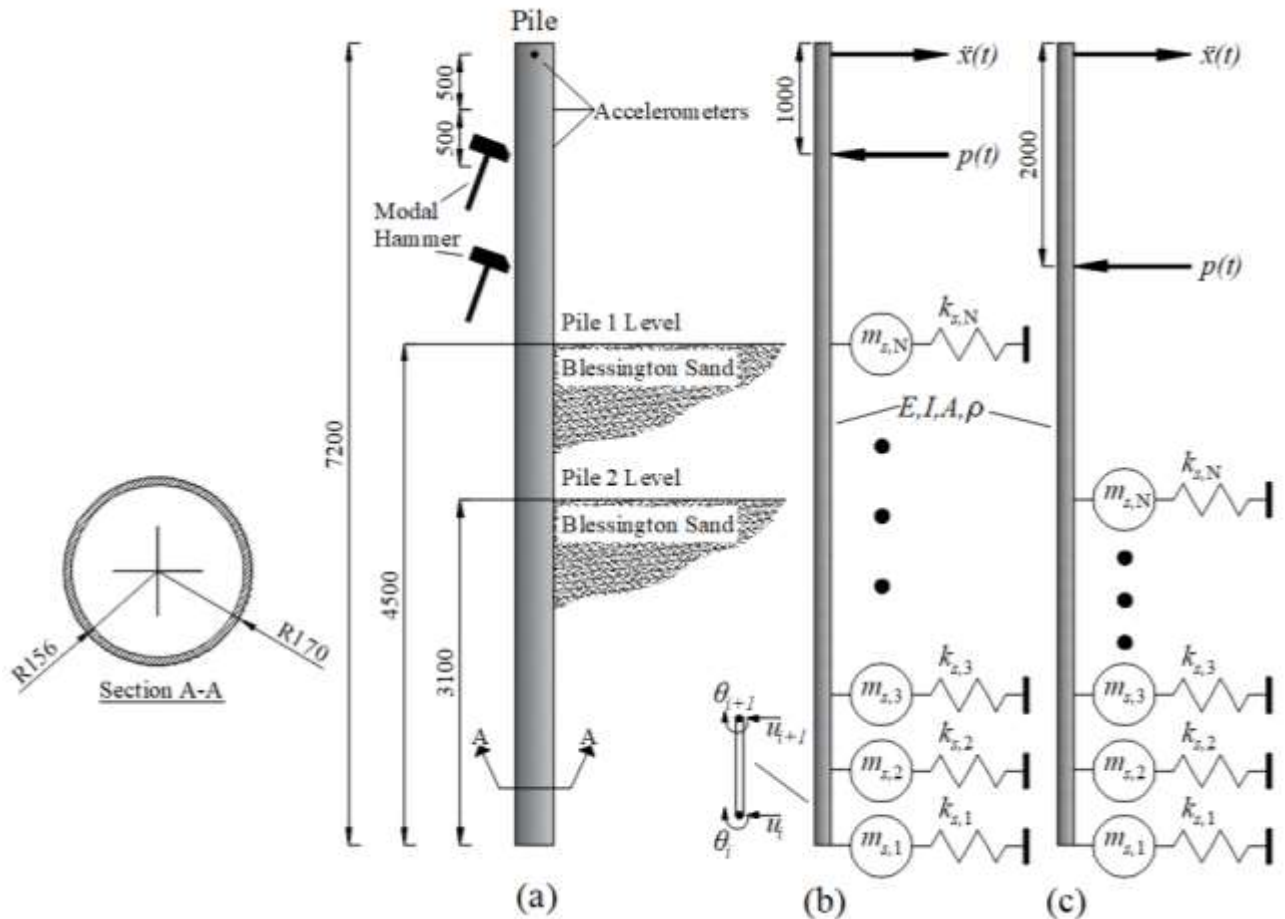
294 5 Analysis

295 5.1 Numerical modelling of field data

296 Two field piles were experimentally tested, as described in Section 4. Two reference numerical
 297 models were developed, shown in Fig. 6(b) and (c) for Pile 1 and 2 respectively, using the procedure
 298 described in Section 2.1. Pile 1 contains 72 Euler-Bernoulli beam elements, each of length 0.1m, and
 299 46 Winkler spring elements to model the soil. Since Pile 1 was initially excavated from an embedment
 300 of 7m to 4.5m, there still exists soil within the pile (as it is an open-ended tube). The level of internal
 301 soil (plug) was approximately 2m below the original ground level. This was incorporated in the
 302 numerical model as an extra mass, assuming a (packed) density for the internal soil at 2000 kg/m^3 .
 303 External soil (added) masses are initially set to zero except for the top quarter of the springs, in line
 304 with the procedure in [23], due to the fact that an embedded pile impacted laterally at the head will
 305 have little modal displacement at depth (Section 5.6 investigates apportioning masses over increasing
 306 portions of the piles). The external impact force is applied at a distance of 1m below the pile head,
 307 close to the point of application on the real system. Pile 2 is modelled similarly to Pile 1, except that
 308 32 Winkler springs are used to model the lesser embedded depth. The soil plug is taken the same as

309 for Pile 1, as an added mass to a depth of 2 m below the original embedded length (i.e. a soil plug 5m
 310 long from the pile tip). The impulse force is applied to a node in the model at a distance of 2m below
 311 the pile head, in accordance to the real situation.

312



313

314 Fig. 6. Model schematic (dimensions in mm), (a) experimental pile geometry, (b) numerical schematic
 315 for Pile 1, (c) numerical schematic for Pile 2

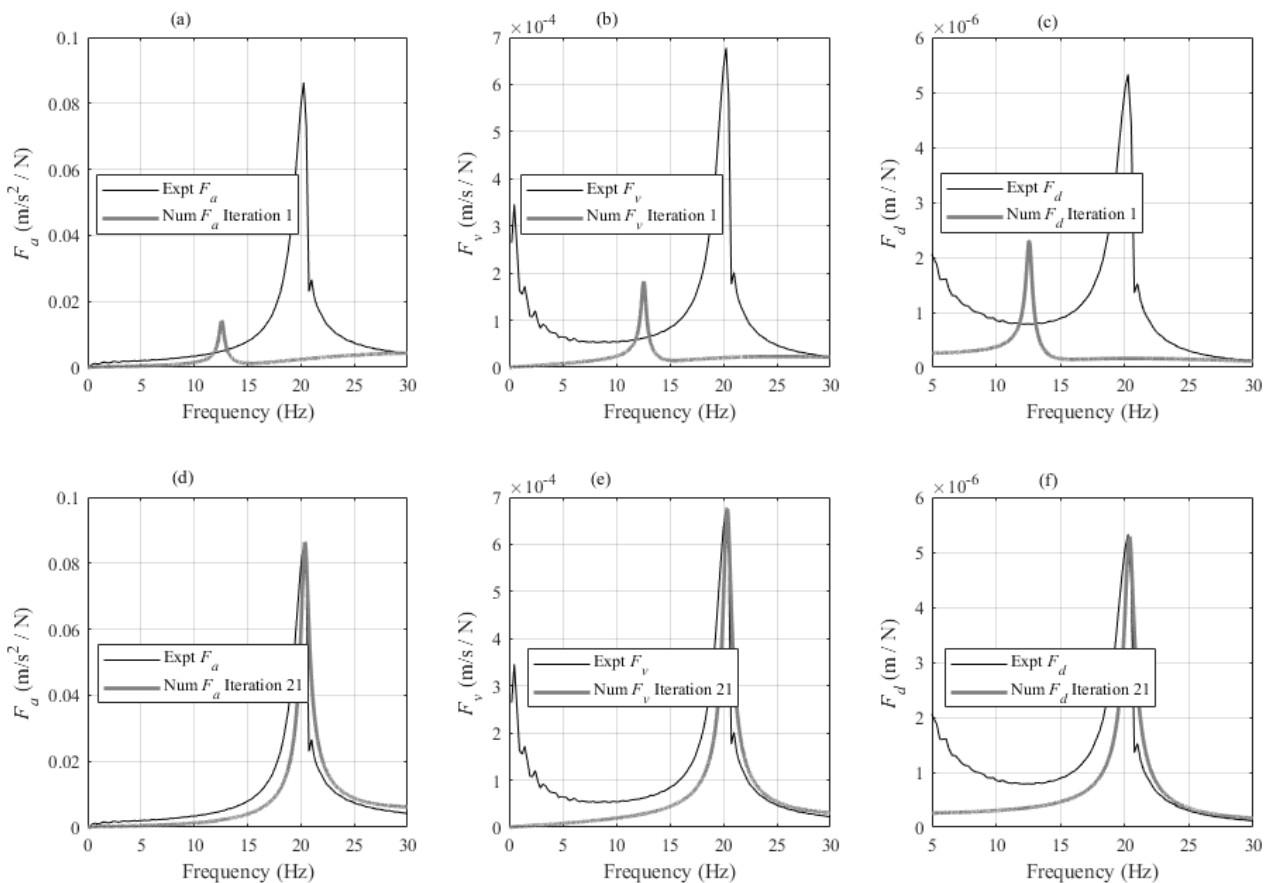
316

317 5.2 Example of applying the iterative updating method

318 An example of running the model is demonstrated in this section and the Pile 1 model with an initial
 319 starting soil stiffness estimate using the Biot approach (Eq. 2) is shown. The results are presented in
 320 Fig. 7 for the first run of the model (with the random starting estimates for mass weighting), and the
 321 final converged values of F_a , since it is the acceleration FRF that is solely used in the procedure, see
 322 Section 3. To show that the method accurately calculates the operating parameters, F_v and F_d are also
 323 shown as calculated in the model overlain on the derived FRFs from the experimental data. Fig. 7(a)
 324 shows the experimental F_a and the first estimate of the numerical F_a . Fig. 7(b) and (c) show the same

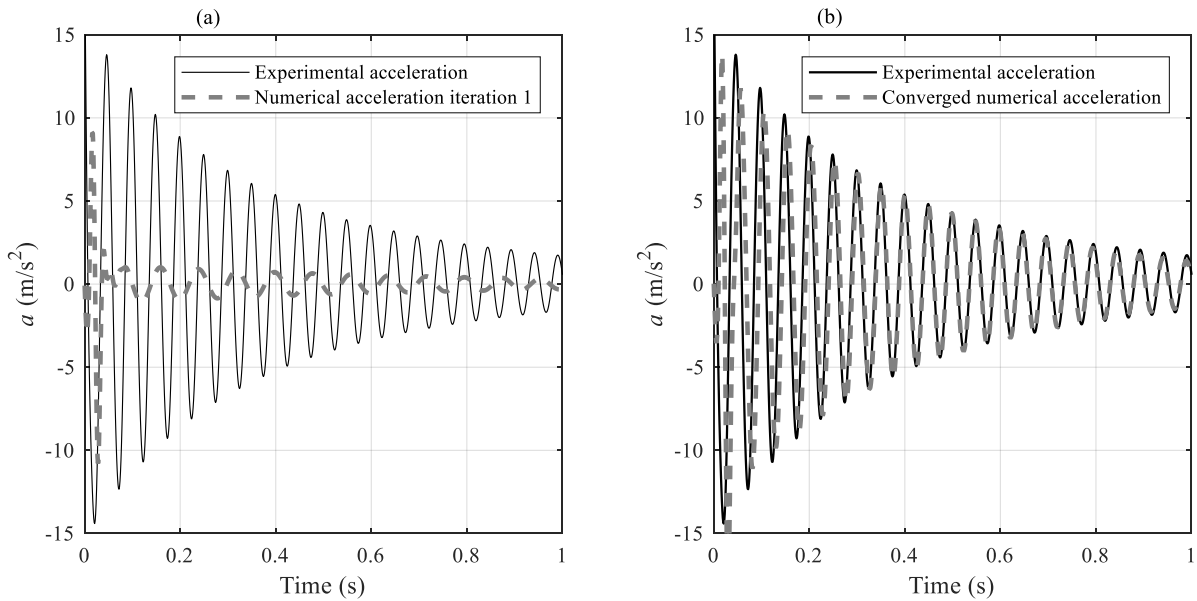
325 information for F_v and F_d respectively. Fig. 7(d) shows the experimental F_a and the converged
 326 numerical F_a . Fig. 7(e) and (f) show the same information for F_v and F_d . A plot of the initial estimate
 327 and final converged acceleration signal, used to develop the numerical F_a is shown in Fig. 8. Fig. 8(a)
 328 shows the predicted acceleration for the first iteration overlain on the experimental signal and
 329 corresponds to the FRFs shown in Fig. 7(a). Fig. 8(b) shows the final converged numerical
 330 acceleration overlain on the experimental signal and corresponds to the FRFs shown in Fig. 7(d). This
 331 figure demonstrates how the approach matches the real-measured response in the time-domain.

332 The method takes 21 iterations to converge (1 global loop of 15 iterations followed by resetting and 6
 333 further iterations). The values of the parameters of interest (mass and stiffness weightings, ratios and
 334 tolerances) for all 21 iterations are reported in Table 2. The method stops when all three tolerances
 335 (mass, frequency and inferred stiffness, see Fig. 1) are less than 0.01 (1%). The method estimates that
 336 the Biot profile applied to the numerical model should be multiplied by 0.95 and soil mass equating to
 337 6 times the pile mass should be distributed to the top quarter of the pile springs in order to match the
 338 experimental FRF.



339

340 Fig. 7. Example of running the method for Biot starting profile – Pile 1. (a) F_a experimental and
 341 numerical iteration 1, (b) F_v experimental and numerical iteration 1, (c) F_d experimental and numerical
 342 iteration 1, (d) F_a experimental and converged numerical, (e) F_v experimental and converged
 343 numerical, (f) F_d experimental and converged numerical.



344

345 Fig. 8 Experimental and predicted accelerations – Pile 1. (a) Iteration 1 of the method, (b) Final
 346 iteration (21) of the method

347

Table 2 Parameters during iterative process

Global loop	Iteration	w_m	w_k	r_m	r_ω	r_k	Tol_m	Tol_ω	Tol_k
0	1	24.442	1.000	6.077	0.621	2.342	5.077	0.379	1.342
0	2	14.442	1.079	2.711	0.802	1.744	1.711	0.198	0.744
0	3	9.359	1.178	1.366	0.965	1.273	0.366	0.035	0.273
0	4	7.974	1.235	1.087	1.025	1.142	0.087	0.025	0.142
0	5	7.542	1.297	0.988	1.055	1.100	0.012	0.055	0.100
0	6	7.592	1.444	0.919	1.089	1.089	0.081	0.089	0.089
0	7	7.533	2.658	0.651	1.273	1.055	0.349	0.273	0.055
0	8	7.611	4.588	0.564	1.400	1.107	0.436	0.400	0.107
0	9	7.220	0.647	1.633	0.834	1.135	0.633	0.166	0.135
0	10	7.451	19.388	0.504	1.641	1.358	0.496	0.641	0.358
0	11	9.023	36.318	0.499	1.718	1.472	0.501	0.718	0.472
0	12	10.250	97.502	0.495	1.821	1.641	0.505	0.821	0.641
0	13	11.206	699.121	0.496	1.970	1.923	0.504	0.970	0.923
0	14	12.402	2236.178	0.498	2.029	2.049	0.502	1.029	1.049

0	15	13.486	10241.427	0.500	2.083	2.169	0.500	1.083	1.169
1	1	2.926	1.000	0.650	1.131	0.831	0.350	0.131	0.169
1	2	12.926	0.867	2.780	0.763	1.620	1.780	0.237	0.620
1	3	4.571	0.971	0.800	1.065	0.908	0.200	0.065	0.092
1	4	5.413	0.958	0.910	1.029	0.964	0.090	0.029	0.036
1	5	6.108	0.949	1.016	1.001	1.018	0.016	0.001	0.018
1	6	6.001	0.952	0.998	1.006	1.009	0.002	0.006	0.009

348

349 **5.3 Converged results for different starting stiffness profiles**

350 In this section, the results of applying each of the five subgrade models (Eqs. 2-6) as the initial
351 starting estimate are trialled for Pile 1 and Pile 2. Each model is run one time, and the results of the
352 converged mass and stiffness weightings for each stiffness profile and both piles are shown in Table
353 3. It is important to note that the converged stiffness weighting should be different for each model, as
354 this is multiplied by the initial profile (Biot, Vesic, etc.) to obtain the converged soil stiffness profile.
355 The mass weighting should be relatively consistent between runs, since this is multiplied by the
356 constant that is the pile mass (for a given pile). In Table 3, it can be seen that for Pile 1, a relatively
357 consistent estimate of the mass weighting is obtained from each model. The converged mass
358 weighting for Pile 2 is a little more variable, though still reasonably consistent.

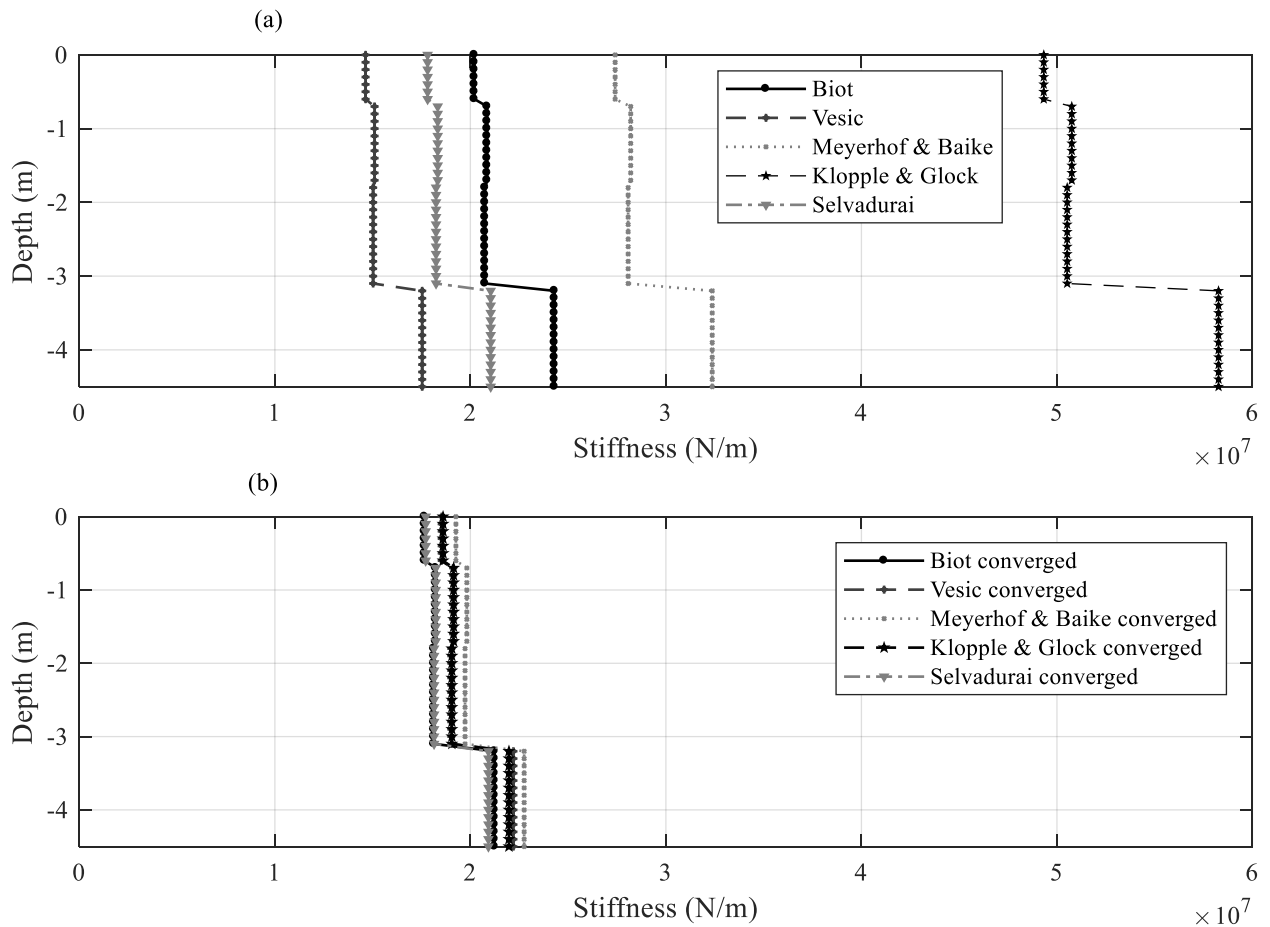
359 Table 3 Converged stiffness and mass weightings for one run of updating method for each subgrade
360 reaction model – Pile 1 & 2

Model	PILE 1		PILE 2	
	Converged w_k	Converged w_m	Converged w_k	Converged w_m
Biot	0.874	5.633	1.779	18.176
Vesic	1.266	5.838	2.399	17.790
Meyerhof & Baike	0.703	5.984	1.369	18.796
Klopple & Glock	0.377	5.858	0.847	20.915
Selvadurai	0.994	5.691	2.101	18.813

361

362 As mentioned above, it is expected the converged stiffness weightings be different for each model, as
363 this is multiplied by the specified soil stiffness profile to obtain the converged stiffness profile. This is

364 best demonstrated as in Fig. 9, which shows the starting and converged stiffness profiles with depth
 365 for each of the five subgrade reaction models for Pile 1. The stiffness is shown in terms of spring
 366 stiffness units (N/m). Fig. 9(a) shows the initial spring stiffness profiles (the markers show the
 367 individual springs) as derived from the site data in Fig. 2(b) using each subgrade model (Eqs. 2-6).
 368 Fig. 9(b) shows the results of multiplying each of these profiles by the associated converged stiffness
 369 weighting for Pile 1 in Table 3. This plot demonstrates visually how the profiles converge toward one
 370 another to establish the *acting* soil stiffness for Pile 1.



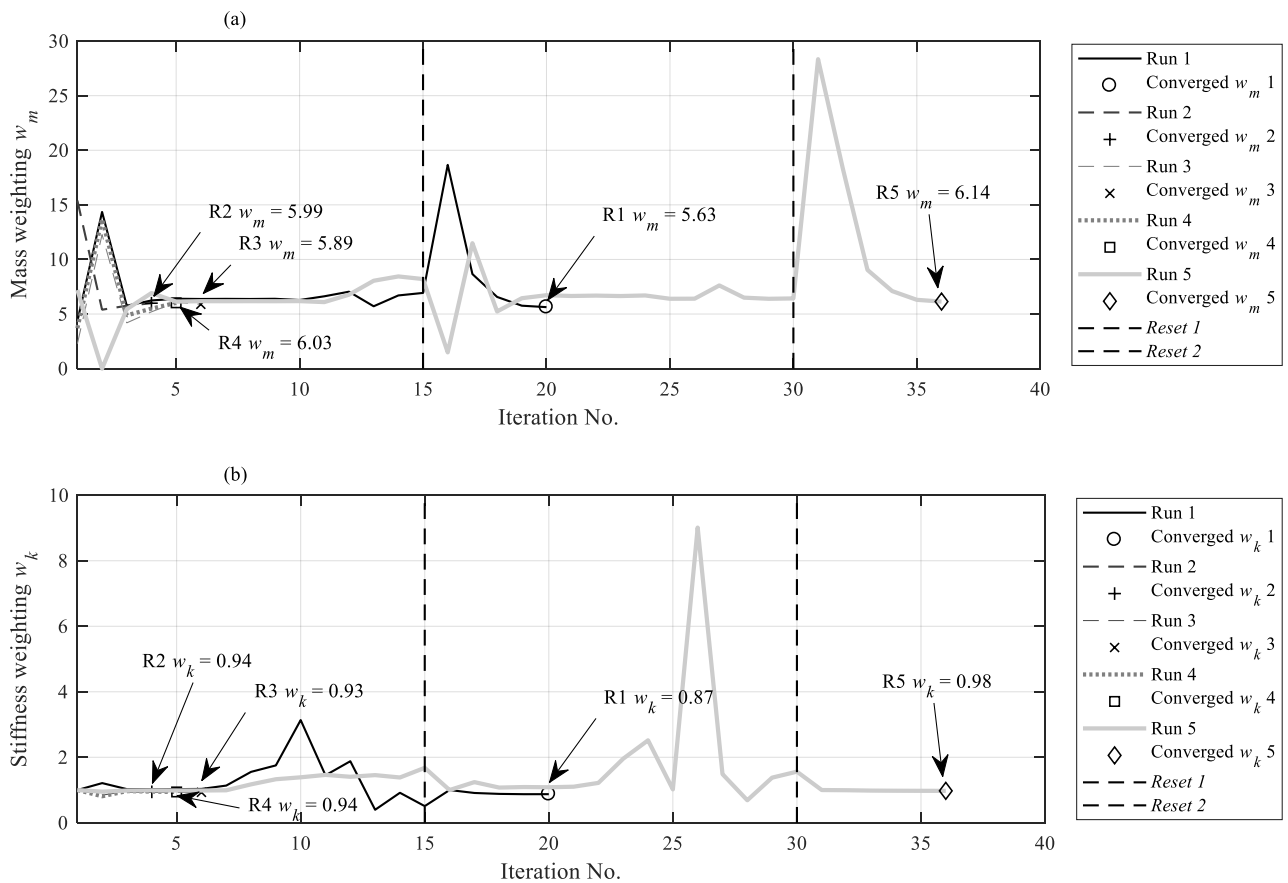
371

372 Fig. 9. Converged stiffness profiles after one run of each model - Pile 1. (a) Original stiffness profiles
 373 from each subgrade reaction formulation, (b) Converged weighted stiffness profile after one run of
 374 each model.

375 5.4 Multiple runs for a given stiffness profile

376 The previous section presents the results of running each model once until convergence is achieved.
 377 However, since each run begins with effectively random starting estimates (between 0 and 30 for the
 378 mass weighting for the first run, and between 0.7 and 1.3 for the stiffness weighting for the second
 379 run), it is of interest to assess repeatability between multiple runs of a given model. Pile 1 with an
 380 initial stiffness profile defined by the Biot model (Eq. 2) is run five times until converged mass and

381 stiffness weightings are obtained. Fig. 10 shows the path of each weighting toward convergence for
 382 each run, Fig. 10(a) for the mass weightings and Fig. 10(b) for the stiffness weightings. Each run (R1-
 383 R5) takes a different number of iterations to converge. R1 takes 20 iteration to converge and ends
 384 with $w_m = 5.63$ and $w_k = 0.87$. R2 takes only 4 iterations to converge and ends with $w_m = 5.99$ and w_k
 385 $= 0.94$. R3 converges after 6 iterations with $w_m = 5.89$ and $w_k = 0.93$. R4 takes 5 iterations and
 386 converges with $w_m = 6.02$ and $w_k = 0.94$. Finally, R5 converges after 36 iterations with $w_m = 6.14$ and
 387 $w_k = 0.98$. Note also that the system resets if convergence is not achieved in 15 iterations, where all
 388 the parameters are reinitialised and the procedure starts over, see Fig. 1. The converged mass and
 389 stiffness weightings do vary a little between runs however in the context of obtaining stiffness
 390 information for geotechnical applications, they are reasonably consistent. Some of the reasons for the
 391 difference in the converged values is discussed in Section 5.7.



392

393 Fig. 10. Results of 5 runs of Biot model – Pile 1. (a) convergence path for mass weighting for 5 runs
 394 of the model, (b) convergence path for stiffness weighting for 5 runs of the model.

395

396 The results for the same analysis on Pile 2 is summarised in Table 4. The mass and stiffness
 397 weightings are reasonably consistent between runs for this pile with the Biot model.

398

399

Table 4 Results of 5 runs of Biot model – Pile 2

Analysis run No.	w_m converged	w_k converged	Iterations
1	18.18	1.78	4
2	18.78	1.85	6
3	18.97	1.86	267
4	18.00	1.78	7
5	19.09	1.87	517

400

401 5.5 Consistency between different experimental impact tests

402 Until now, only one set of experimental data from each pile, namely F_a from 1 impact test (P1 T1 and
 403 P2 T1 Table 1) has been considered. In this section, the ability for the method to calculate consistent
 404 mobilised stiffness and mass weightings from a number of impact tests conducted on both Piles 1 and
 405 2 is evaluated. The target FRFs for five impact tests are shown in Fig. 4. The method is run one time
 406 for each of the starting soil stiffness models (Eqs. 2-6), for each of the five impact tests conducted on
 407 both piles (Table 1), resulting in a total of 50 runs. Table 5 shows the values of the converged stiffness
 408 and mass weightings from each run for Pile 1 and Table 6 shows the results for Pile 2.

409

Table 5 Pile 1 Analysis of five impact tests

Impact Test No.	VESIC		SELVADURAI		BIOT		MEYERHOF		KLOPPLE	
	w_m	w_k	w_m	w_k	w_m	w_k	w_m	w_k	w_m	w_k
1	5.838	1.266	5.691	0.994	5.633	0.874	5.984	0.703	5.858	0.377
2	4.570	1.007	5.112	0.939	5.233	0.847	4.767	0.569	4.731	0.312
3	3.861	0.963	3.661	0.750	3.774	0.680	3.661	0.484	3.684	0.270
4	4.179	1.000	4.058	0.775	4.125	0.704	4.110	0.518	4.006	0.276
5	3.316	0.874	3.152	0.684	3.391	0.638	3.237	0.451	3.265	0.252

410

411

Table 6 Pile 2 Analysis of five impact tests

Impact Test No.	VESIC		SELVADURAI		BIOT		MEYERHOF		KLOPPLE	
	w_m	w_k	w_m	w_k	w_m	w_k	w_m	w_k	w_m	w_k
1	17.790	2.399	18.813	2.101	18.176	1.779	18.796	1.369	20.915	0.847
2	16.763	2.375	16.203	1.881	18.413	1.829	17.606	1.323	17.862	0.738
3	17.959	2.486	17.918	2.045	17.771	1.790	17.991	1.334	17.649	0.710
4	15.771	2.366	15.625	1.905	15.371	1.670	14.932	1.199	16.107	0.708
5	15.220	2.030	15.376	1.686	14.249	1.379	15.757	1.104	15.633	0.622

412

413 Observing Table 5 and 6, the data from different impact tests lead to slightly different estimates of
 414 converged mass weightings in each case, for both piles. It is noteworthy that for a given impact test,
 415 the converged mass weightings for each of the soil stiffness models are relatively consistent for a
 416 given pile. There are two potential reasons for this, (i) the mass weighting is very sensitive to the
 417 quality of F_a and any variations in this strongly affect the converged mass weighting, or (ii) depending
 418 on the magnitude of the impact applied in each case, different amounts of mass may have been
 419 mobilised in the soil surrounding the pile. Converged stiffness weightings for a given soil profile also
 420 vary somewhat between impact tests. Further potential reasons for these differences are discussed in
 421 Section 5.7.

422 **5.6 Influence of changing the active length over which masses are apportioned**

423 All previous analyses consider the added soil masses apportioned to the top quarter of the springs in
 424 each model, as an approximate estimate for the mobilised mass of soil contributing to the first mode
 425 of vibration of each system. In reality, there will be some depth over which the soil mass will be
 426 effectively mobilised, due to the nature of the pile head bending when impacted. The active length, or
 427 effective depth of a pile, is the length beyond which further increases in pile length do not have any
 428 additional influence on pile head displacements, or rotations (or frequency) [52]. Quantifying the
 429 active length is an area of much uncertainty and previous studies have suggested several formulations
 430 for this parameter, which vary depending on the constraints applied to the pile head, the pile rigidity,
 431 and the nature of applied loading [53–58]. In this section, the influence of distributing masses over
 432 different lengths of a pile on the converged stiffness and mass weightings is studied. Active lengths
 433 equating to 25%, 50%, 75% and 100% of the embedded pile length are considered. Pile 1 impact test
 434 1 (P1 T1, Table 1) is used as the test case and a Biot soil profile is adopted as the initial soil stiffness
 435 estimate. Each model is run five times for a given mass length distribution, and the results are
 436 presented in Table 7 as the average \pm standard deviation of converged mass and stiffness weightings,
 437 for each mass distribution case.

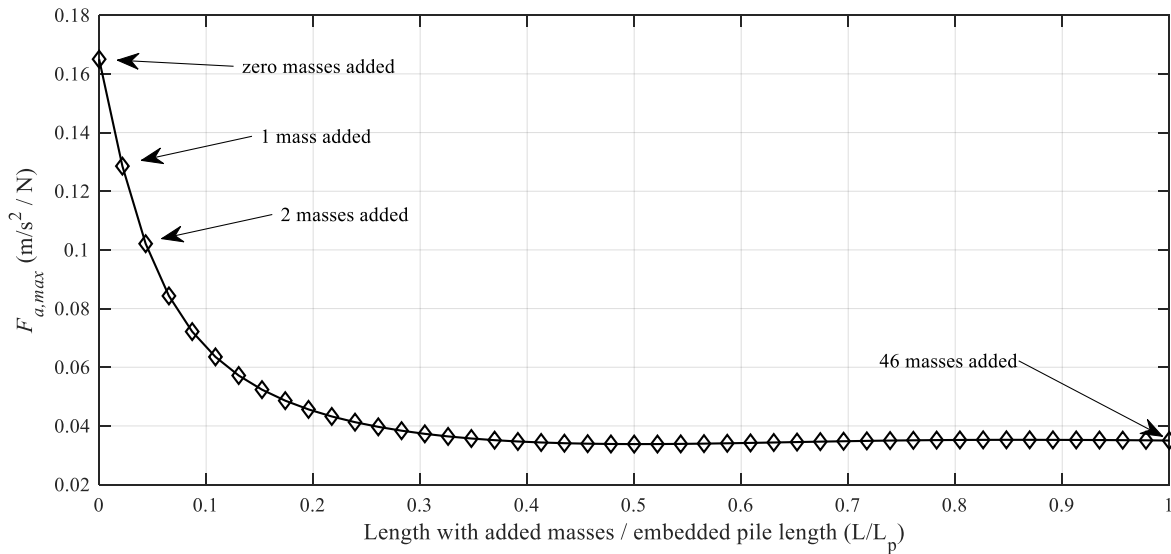
438 Table 7 Influence of mass length distribution on converged weightings

Masses distributed over length, L (L_p = pile length)	Average $w_m \pm$ Standard deviation	Average $w_k \pm$ Standard deviation
L=0.25L_p	5.83±0.27	0.92±0.05
L=0.5L_p	11.54±0.39	0.92±0.04
L=0.75L_p	18.10±0.70	0.97±0.04
L=L_p	23.90±0.44	0.97±0.02

439

440 Increasing the length over which masses are apportioned has limited influence on the converged
441 stiffness weighting, with these values remaining sufficiently consistent for each case, considering the
442 nominal errors present due to the natural variability in the algorithm convergence process. However,
443 the converged mass weighting increases proportionally to the increase in mass distribution length,
444 changing from $w_m=5.83$ for masses distributed over 25% of the pile embedment to $w_m=23.90$ for
445 masses distributed along the entire embedded depth. In the procedure to add point masses to the pile,
446 the mass weighting is multiplied by a fixed ‘added mass’, which is the pile mass, and this is then
447 divided equally among the ‘active spring nodes’, namely the nodes with non-zero added masses. So,
448 for the first case, a weighting of 5.83 is multiplied by the pile mass and divided among 12 springs (a
449 quarter of the 46 springs), giving ≈ 0.5 times the pile mass added to each spring. For the last case, a
450 pile weighting of 23.90 is multiplied by the pile mass and divided among all 46 springs, again giving
451 ≈ 0.5 times the pile mass added to each spring. Therefore, when one normalises the converged
452 weighting to the number of springs with non-zero added masses, the added point mass at each spring
453 is approximately the same.

454 This finding highlights that no matter how many springs are specified to attach masses, the added
455 point mass at each spring will be approximately the same. This result may seem counterintuitive as
456 the global mass added increases with the number of active springs, and suggests that the approach is
457 therefore very sensitive to the specified active length by the user. However, this result may be
458 understood by observing the influence of added point masses on the F_a peak height for the first mode
459 of the pile. Herein, the model for Pile 1 with a Biot stiffness profile subjected to an impact test is
460 shown for the case where fixed point masses are added sequentially to the springs starting from
461 ground level. The first run contains no added soil mass, the second run has one added mass, etc., until
462 all the springs contain the same added point mass. With the increasing number of added masses, the
463 FRF F_a peak height ($F_{a,max}$) decreases logarithmically, see Fig. 11. It is noteworthy that the peak
464 heights, $F_{a,max}$ for the cases with masses added to 12 springs ($L/L_p=0.25$) and masses added to 46
465 springs ($L/L_p=1$) do not vary significantly, which explains why the result appears insensitive to the
466 length over which masses are added. Note, to further investigate this influence would require
467 observing higher modes of vibration, which would be influenced strongly by a given mass
468 distribution. However, this is beyond the scope of the present study. It is recommended that potential
469 users of the method specify an active length using the most applicable approach available.



470

471 Fig. 11 Influence of increasing the number of added masses along the pile on the F_a peak value

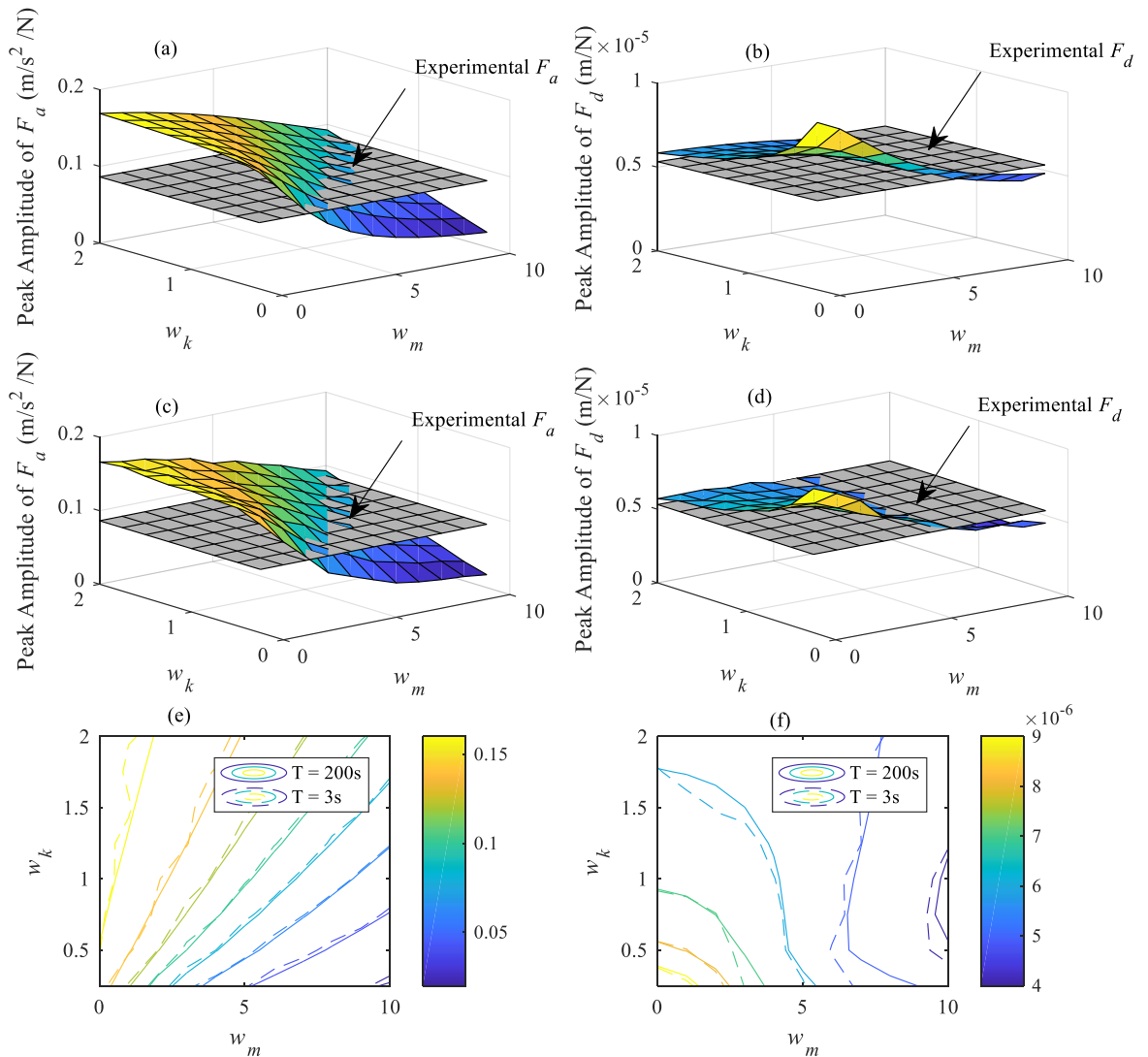
472

473 **5.7 Sources of error in the method**

474 The iterative model updating approach presented in [23] was developed and validated using
 475 numerically simulated data of piles. Application of the approach to real experimental data has
 476 unearthed some issues. Variability and noise in experimental data inevitably affects the quality of
 477 results. One of the key issues may relate to the time-length of the signals available for the
 478 experimental analysis. The impact tests conducted on both piles contained 3 seconds of acceleration
 479 data. The impact of this is investigated in Figs. 12 and 13. Fig. 12(a) shows how the FRF F_a peak
 480 amplitude varies for different mass and stiffness weightings applied to the numerical model of Pile 1
 481 with a Biot soil stiffness profile. The surface plot in Fig. 12(a) is generated using time signals of
 482 length $T=200s$, the same as the analyses conducted throughout this paper. Also shown as a horizontal
 483 plane in grey is the peak amplitude of the experimental F_a as measured in the first impact test on Pile
 484 1. An immediately obvious trait is that the numerical F_a peak amplitude is affected by changes in both
 485 mass and stiffness weighting, which deviates significantly from the theory of how single-degree-of-
 486 freedom (SDOF) models should behave, see [23]. The curve along which both the experimental and
 487 numerical planes intersect provides the solution combinations $\{w_m, w_k\}$, which lead to the same F_a
 488 peak amplitude in the numerical model as in the experimental data. It is important to note that the
 489 other criterion of matching the frequency is required in the iterative procedure, but not shown in these
 490 plots. This explains why the procedure always converges on broadly similar values for a given
 491 situation, and not a large range, as would be the case if the F_a peak alone were sought. Fig. 12(b)
 492 shows the same information as Fig. 12(a) but this time for the FRF F_d peak amplitude. The
 493 experimental data (horizontal grey plane) is the F_d peak amplitude derived from the experimental F_a

494 using Eq. (9). Once again there is an intersection curve of $\{w_m, w_k\}$ combinations that enables the
495 numerical model have the same F_d as the experiment. The influence of time on signal quality is
496 investigated in Figs. 12(c) and (d), where an acceleration time series of length $T=3s$ is used for each
497 run. The difference between the surface plots in (a) and (b) to those in (c) and (d) is best demonstrated
498 in the contour plots shown in Fig. 12(e) and (f). The result of using a time series of length $T=200s$ for
499 the analyses is shown by the smoothness of the solid contour lines in parts (e) and (f). Reducing the
500 time series to $T=3s$ (in line with the experimental data) leads to a more jagged contour plot, denoted
501 by the dashed lines in (e) and (f). This roughness in the peak F_a amplitude infers that for convergence
502 to be achieved between the ‘rough’ experimental F_a and the ‘smooth’ numerical F_a some errors are
503 introduced. For Pile 1 with a Biot stiffness profile, this is quite minor, however Fig. 13 shows the
504 same information for Pile 2, which is significantly affected by signal length issues.

505



506

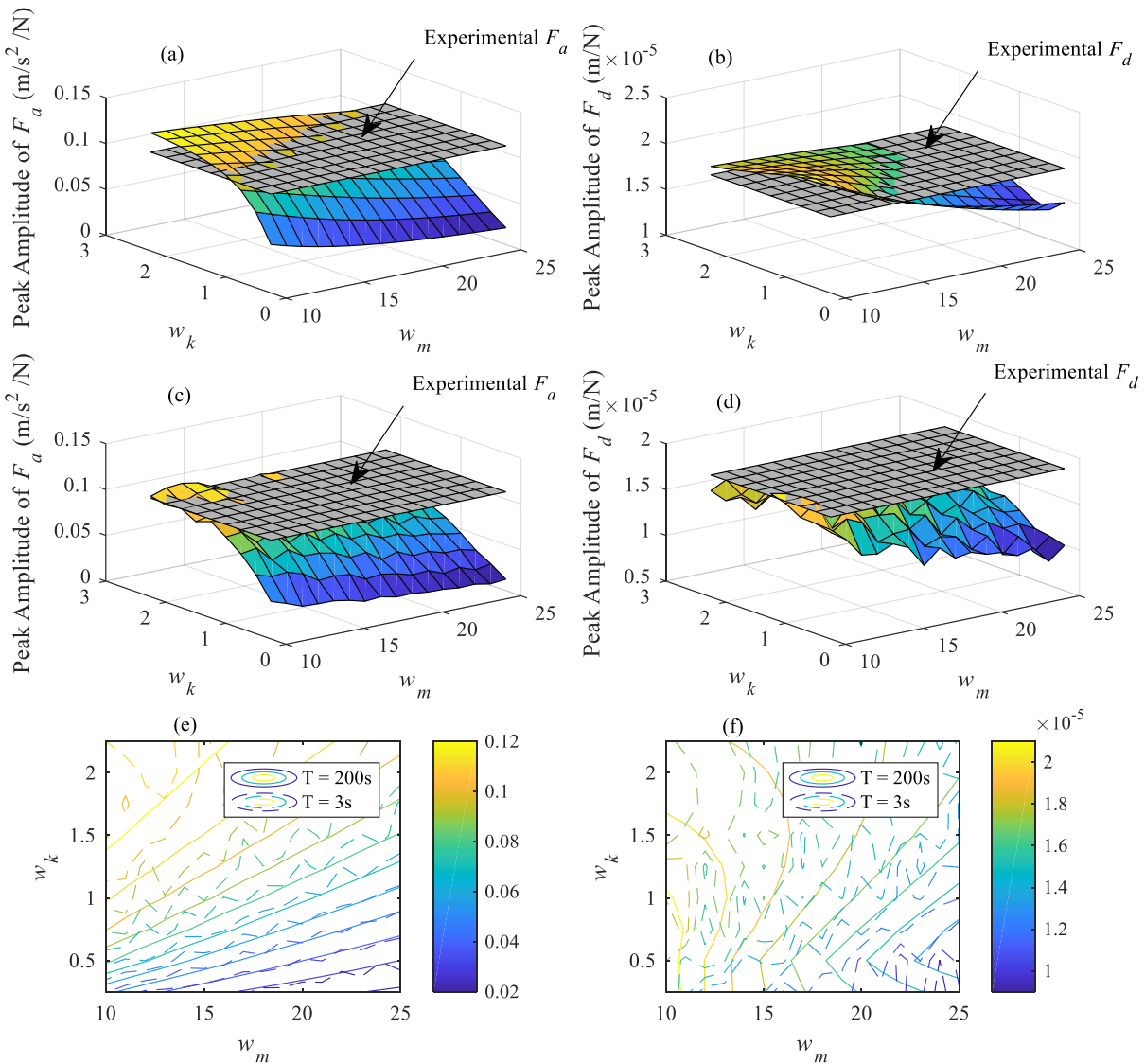
507 Fig. 12. Influence of signal length on FRF peak height for different mass and stiffness weightings for
 508 Pile 1 – Biot model. (a) variation of peak amplitude of F_a with w_m and w_k compared to experimental F_a
 509 Impact Test 1 – $T=200s$, (b) variation of peak amplitude of F_d with w_m and w_k compared to
 510 experimental F_d (derived) Impact Test 1 – $T=200s$, (c) variation of peak amplitude of F_a with w_m and
 511 w_k compared to experimental F_a Impact Test 1 – $T=3s$, (b) variation of peak amplitude of F_d with w_m
 512 and w_k compared to experimental F_d (derived) Impact Test 1 – $T=3s$, (e) contour plot of peak
 513 amplitude of F_a with w_m and w_k for both $T=200s$ and $T=3s$ runs, (d) contour plot of peak amplitude of
 514 F_d with w_m and w_k for both $T=200s$ and $T=3s$ runs.

515

516 Fig. 13 shows the results for Pile 2 with a Biot soil stiffness profile. Fig. 13(a) shows a surface plot of
 517 the F_a peak amplitude and how it varies with mass and stiffness weightings. Fig. 13(b) shows this
 518 information for the F_d peak amplitude. Also shown as a horizontal grey plane is the experimental F_a
 519 peak amplitude in (a) and derived F_d peak amplitude in (b) from the first impact test on Pile 2. The

520 smooth surface plots in (a) and (b) are derived from analysis of signals that are $T=200$ s long. Figs.
 521 13(c) and (d) show the same information as (a) and (b) respectively, but are generated from time
 522 signals that are $T=3$ s long. For this case there is a substantial decrease in the smoothness of each plot,
 523 which highlights the potential errors that are introduced by the use of short time signals in the
 524 experimental data analysis. The results from the four surface plots in Figs. 13(a)-(d) are shown as
 525 contour plots in (e) and (f), where the solid contours are generated from $T=200$ s signals and the
 526 jagged contours from $T=3$ s. This highlights that use of the short experimental signals is a potential
 527 source of model error, which may be significant. This may account for some of the difference in
 528 calculated stiffness weightings between Pile 1 and 2. Note, all of the analyses in the previous sections
 529 used $T=200$ s for the numerical modelling while the experimental signals contained only 3 seconds of
 530 data.

531



532

533 Fig. 13. Influence of signal length on FRF peak height for different mass and stiffness weightings for
 534 Pile 2 – Biot model. (a) variation of peak amplitude of F_a with w_m and w_k compared to experimental F_a
 535 Impact Test 1 – $T=200$ s, (b) variation of peak amplitude of F_d with w_m and w_k compared to
 536 experimental F_d (derived) Impact Test 1 – $T=200$ s, (c) variation of peak amplitude of F_a with w_m and
 537 w_k compared to experimental F_a Impact Test 1 – $T=3$ s, (b) variation of peak amplitude of F_d with w_m
 538 and w_k compared to experimental F_d (derived) Impact Test 1 – $T=3$ s, (e) contour plot of peak
 539 amplitude of F_a with w_m and w_k for both $T=200$ s and $T=3$ s runs, (d) contour plot of peak amplitude of
 540 F_d with w_m and w_k for both $T=200$ s and $T=3$ s runs.

541 While the short time-length of the processed signals may be the largest source of error, an additional
 542 source of error arises from the experimental impact testing. Each pile is an open-ended steel cylinder
 543 and, when subjected to impacts from a modal hammer, this induces an in-plane excitation in the pile
 544 annulus. This in-plane excitation manifests as a high-frequency pollution in the bending signal. Prior
 545 to transforming the time-signal to a FRF, the signal is low-pass filtered to remove the contribution of
 546 this noise [6,41]. This process will have some influence on the quality and nature of the FRF.

547 Further sources of error might arise due to the stepped nature of the available soil stiffness (E) data
 548 from the multi-channel analysis of surface waves. Any errors here may be exacerbated in the
 549 procedure, which uses a single stiffness weighting for the entire profile depth. Moreover, since Pile 2
 550 has less embedded depth than Pile 1, any errors in this profile will be exacerbated further. It should be
 551 noted that the same E profile is used for both piles, as this is in effect an average profile for the test
 552 site, so some errors can be expected as to the actual acting magnitudes at each depth. In terms of the
 553 *reference* numerical models developed, there is some question over the mass density of the internal
 554 plugged soil in each pile, which had to be estimated for the purposes of this paper. Additionally, the
 555 numerical method involves simplifying the pile to a 1D beam-Winkler system, which may deviate in
 556 behaviour from the real continuous pile system. Due to numerical constraints in iterative analyses of
 557 this nature, it is infeasible to use a full 3D model as it would be computationally too expensive.

558 6. Conclusion

559 In this paper, the application of a finite-element model updating approach to estimating the mobilised
 560 soil stiffness and mass in laterally impacted piles is studied. The reason behind the development of
 561 this method is due to the ongoing uncertainty surrounding the specification of soil-structure
 562 interaction stiffness in pile-soil interaction. Moreover, any contribution of soil mass is typically
 563 ignored. The method, which was previously derived and applied to simulated data, is demonstrated
 564 using experimental pile data in this paper.

565 Impact tests are performed on two piles with varying L/D ratios to derive frequency response
 566 functions, which are used as the target in an algorithm to estimate the mobilised soil stiffness and
 567 mass. Five subgrade reaction formulations are used to specify the initial starting stiffness. The
 568 analysis updates the soil stiffness and mass in a numerical model of the pile to converge on the

569 experimental FRF. For the case where each of the five subgrade reaction models are used, the method
570 converges on broadly similar added mass weightings and the converged stiffness profiles are
571 relatively similar. This is better for Pile 1 than for Pile 2, which exhibits more variability (less
572 embedded depth leads to more errors potentially). For a given impact test, the effect of running the
573 model multiple times is studied to ascertain if significant variability exists between different runs. The
574 results do vary a little, due to the random nature of the starting estimates for mass in the first iteration
575 and stiffness in the second iteration, though the converged values are broadly similar for each trial.
576 More variability is evident when different impact tests are used as the target FRF for each case. In
577 general, for a given impact test, the converged mass weighting for each subgrade reaction model is
578 relatively similar for a given pile. However, the difference between the converged weightings for the
579 different impact tests warrants some discussion. Experimental errors in the FRF peak height is most
580 likely the reason for this variation, though there is potentially some influence from the amount of
581 mobilised mass surrounding the pile as a result of the intensity of a given impact from the modal
582 hammer. Additionally, the influence of the active depth over which masses are distributed is also
583 investigated and it is shown for the conditions tested that masses distributed over a length beyond
584 20% of the embedment have limited further influence on the first mode of vibration. However, the
585 effect on higher modes was not evaluated and would require further study. Finally, the sources of
586 error due to time-length of signals is studied with a view to shedding some light on the importance of
587 accurate experimental data. It is recommended that future studies use longer time signals for the
588 experimental data than those available in the present study to mitigate against these signal-processing
589 related issues. Short time signals lead to poorly spaced frequency vectors in the FRF, which may
590 strongly influence the converged results.

591 Aside from some issues, the method was applied with relative success in this paper, and shows that a
592 simple impact test may be useful to obtain better estimates of the mobilised soil-structure interaction
593 stiffnesses and masses acting in the small-strain dynamic soil-pile behaviour. The research may be
594 useful for the development of more accurate damage quantification models for SSI applications or in
595 the growing offshore monopile fields.

596 Future work will investigate extension of the approach to use of multiple vibration modes to provide
597 further insight into the behaviour and, to potentially enable depth-dependant weightings be obtained.
598 The latter may be more useful for cases where large-strain deformations are experienced at pile heads
599 relative to at-depth, thereby enabling calculation of the mobilised strain-dependant stiffness at the pile
600 head. Furthermore, expansion of the approach to different types of foundation structures such as
601 shallow pads or suction caissons should form part of future work. It should be noted that the approach
602 in this paper uses an impact from a modal hammer to excite a structure; therefore there are some
603 limitations of this approach. Large-diameter monopiles may not be sufficiently excited by impact
604 from a modal hammer in order to obtain reliable FRFs. Moreover, highly damped systems suffer the

605 same issues. Expansion of the approach to these types of systems may require investigation of
606 different excitation sources to generate FRFs.

607 **Acknowledgements**

608 This research was enabled through funding obtained from the Royal Irish Academy Charlemont
609 Scholarship Research Travel Awards 2016.

610 **References**

- 611 [1] Kampitsis AE, Sapountzakis EJ, Giannakos SK, Gerolymos N a. Seismic soil–pile–structure
612 kinematic and inertial interaction—A new beam approach. *Soil Dyn Earthq Eng* 2013;55:211–
613 24. doi:10.1016/j.soildyn.2013.09.023.
- 614 [2] Boulanger RW, Curras CJ, Kutter BL, Wilson DW, Abghari A. Seismic soil-pile-structure
615 interaction experiments and analysis. *J Geotech Geoenvironmental Eng* 1999;125:750–9.
- 616 [3] Prendergast LJ, Reale C, Gavin K. Probabilistic examination of the change in eigenfrequencies
617 of an offshore wind turbine under progressive scour incorporating soil spatial variability. *Mar*
618 *Struct* 2018;57:87–104. doi:10.1016/j.marstruc.2017.09.009.
- 619 [4] Versteijlen WG, Metrikine AV, van Dalen KN. A method for identification of an effective
620 Winkler foundation for large-diameter offshore wind turbine support structures based on in-
621 situ measured small-strain soil response and 3D modelling. *Eng Struct* 2016;124:221–36.
622 doi:10.1016/j.engstruct.2016.06.007.
- 623 [5] Allotey N, El Naggar MH. Generalized dynamic Winkler model for nonlinear soil–structure
624 interaction analysis. *Can Geotech J* 2008;45:560–73. doi:10.1139/T07-106.
- 625 [6] Prendergast LJ, Gavin K. A comparison of initial stiffness formulations for small-strain soil –
626 pile dynamic Winkler modelling. *Soil Dyn Earthq Eng* 2016;81:27–41.
627 doi:10.1016/j.soildyn.2015.11.006.
- 628 [7] Zhu XQ, Law SS. Wavelet-based crack identification of bridge beam from operational
629 deflection time history. *Int J Solids Struct* 2006;43:2299–317.
630 doi:10.1016/j.ijsolstr.2005.07.024.
- 631 [8] Domaneschi M, Limongelli M, Martinelli L. Vibration based damage localization using
632 MEMS on a suspension bridge model. *Smart Struct* 2013;12:679–94.
- 633 [9] OBrien E, Malekjafarian A. A mode shape-based damage detection approach using laser
634 measurement from a vehicle crossing a simply supported bridge. *Struct Control Heal Monit*
635 2016.
- 636 [10] Prendergast LJ, Hester D, Gavin K. Determining the presence of scour around bridge

- 637 foundations using vehicle-induced vibrations. *J Bridg Eng* 2016;21.
638 doi:10.1061/(ASCE)BE.1943-5592.0000931.
- 639 [11] Foti S, Sabia D. Influence of Foundation Scour on the Dynamic Response of an Existing
640 Bridge. *J Bridg Eng* 2011;16:295–304. doi:10.1061/(ASCE)BE.1943-5592.0000146.
- 641 [12] Briaud JL, Hurlbauss S, Chang K, Yao C, Sharma H, Yu O, et al. Realtime monitoring of
642 bridge scour using remote monitoring technology. vol. 7. Austin, TX: 2011.
- 643 [13] Prendergast LJ, Hester D, Gavin K. Development of a Vehicle-Bridge-Soil Dynamic
644 Interaction Model for Scour Damage Modelling. *Shock Vib* 2016;2016.
645 doi:10.1155/2016/7871089.
- 646 [14] Chen C-C, Wu W-H, Shih F, Wang S-W. Scour evaluation for foundation of a cable-stayed
647 bridge based on ambient vibration measurements of superstructure. *NDT E Int* 2014;66:16–27.
648 doi:10.1016/j.ndteint.2014.04.005.
- 649 [15] Imregun M, Visser WJ, Ewins. Finite Element Model Updating Using Frequency Response
650 Function Data—I. Theory and Initial Investigation. *Mech Syst Signal Process* 1995;9:187–
651 202. doi:DOI: 10.1006/mssp.1995.0015.
- 652 [16] Nalitlela N, Penny JET, Friswell MI. Updating Model Parameters By Adding an Imagined
653 Stiffness To the Structure. *Mech Syst Signal Process* 1993;7:161–72.
654 doi:10.1006/mssp.1993.1005.
- 655 [17] Mottershead JE, Link M, Friswell MI. The sensitivity method in finite element model
656 updating: A tutorial. *Mech Syst Signal Process* 2011;25:2275–96.
657 doi:10.1016/j.ymsp.2010.10.012.
- 658 [18] Hwang HY, Kim C. Damage detection in structures using a few frequency response
659 measurements. *J Sound Vib* 2004;270:1–14. doi:10.1016/S0022-460X(03)00190-1.
- 660 [19] Mottershead JE, Friswell MI. Model Updating In Structural Dynamics: A Survey. *J Sound Vib*
661 1993;167:347–75. doi:10.1006/jsvi.1993.1340.
- 662 [20] Esfandiari A, Bakhtiari-Nejad F, Rahai A, Sanayei M. Structural model updating using
663 frequency response function and quasi-linear sensitivity equation. *J Sound Vib* 2009;326:557–
664 73. doi:10.1016/j.jsv.2009.07.001.
- 665 [21] Lin RM, Zhu J. Model updating of damped structures using FRF data. *Mech Syst Signal*
666 *Process* 2006;20:2200–18. doi:10.1016/j.ymsp.2006.05.008.
- 667 [22] Lin RM, Ewins DJ. Analytical model improvement using frequency response functions. *Mech*
668 *Syst Signal Process* 1994;8:437–58. doi:10.1006/mssp.1994.1032.
- 669 [23] Wu WH, Prendergast LJ, Gavin K. An iterative method to infer distributed mass and stiffness

- 670 profiles for use in reference dynamic beam-Winkler models of foundation piles from
 671 frequency response functions. *J Sound Vib* 2018;431:1–19. doi:10.1016/j.jsv.2018.05.049.
- 672 [24] Kwon YW, Bang H. *The Finite Element Method using MATLAB*. Boca Raton, FL: CRC
 673 Press, Inc.; 2000.
- 674 [25] Winkler E. *Theory of elasticity and strength*. Dominicus Prague: 1867.
- 675 [26] Dutta SC, Roy R. A critical review on idealization and modeling for interaction among soil–
 676 foundation–structure system. *Comput Struct* 2002;80:1579–94. doi:10.1016/S0045-
 677 7949(02)00115-3.
- 678 [27] Clough RW, Penzien J. *Dynamics of structures*. 1993.
- 679 [28] Tedesco JW, McDougal WG, Allen Ross C. *Structural Dynamics: Theory and Applications*.
 680 1999.
- 681 [29] Dukkipati RV. *Matlab for Mechanical Engineers*. New Age Science; 2009.
- 682 [30] Biot MA. Bending of an infinite beam on an elastic foundation. *J Appl Mech* 1937;59:A1–7.
- 683 [31] Vesic AB. Bending of beams resting on isotropic elastic solid. *J Soil Mech Found Eng*
 684 1961;87:35–53.
- 685 [32] Ashford SA, Juirnarongrit T. Evaluation of Pile Diameter Effect on Initial Modulus of
 686 Subgrade Reaction. *Geotech Geoenvironmental Eng* 2003;129:234–42.
 687 doi:10.1061/(ASCE)1090-0241(2003)129:3(234).
- 688 [33] Okeagu B, Abdel-Sayed G. Coefficients of Soil Reaction for Buried Flexible Conduits. *J*
 689 *Geotech Eng* 1984;110:908–22. doi:10.1061/(ASCE)0733-9410(1984)110:7(908).
- 690 [34] Sadrekarimi J, Akbarzad M. Comparative Study of Methods of Determination of Coefficient
 691 of Subgrade Reaction. *Electron J Geotech Eng* 2009;14.
- 692 [35] Elachachi SM, Breyse D, Houy L. Longitudinal variability of soils and structural response of
 693 sewer networks. *Comput Geotech* 2004;31:625–41. doi:10.1016/j.compgeo.2004.10.003.
- 694 [36] Donohue S, Long M, Gavin K, O’Connor P. Shear Wave Stiffness of Irish Glacial Till. *Int.*
 695 *Conf. Site Characterisation I*, Porto, Portugal: 2004, p. 459–66.
- 696 [37] Prendergast LJ, Hester D, Gavin K, O’Sullivan JJ. An investigation of the changes in the
 697 natural frequency of a pile affected by scour. *J Sound Vib* 2013;332:6685–702.
 698 doi:http://dx.doi.org/10.1016/j.jsv.2013.08.020i.
- 699 [38] Fugro. *Guide for Estimating Soil Type and Characteristics using Cone Penetration Testing*.
 700 *Cone Penetration Tests* 2011. <http://www.fes.co.uk/downloads/CPT-general.pdf> (accessed
 701 May 12, 2014).

- 702 [39] Qi WG, Gao FP, Randolph MF, Lehane BM. Scour effects on p - y curves for shallowly
 703 embedded piles in sand. *Géotechnique* 2016;66:648–60. doi:10.1680/jgeot.15.P.157.
- 704 [40] Prendergast LJ, Gavin K, Doherty P. An investigation into the effect of scour on the natural
 705 frequency of an offshore wind turbine. *Ocean Eng* 2015;101:1–11.
 706 doi:10.1016/j.oceaneng.2015.04.017.
- 707 [41] Dezi F, Gara F, Roia D. Dynamic response of a near-shore pile to lateral impact load. *Soil Dyn*
 708 *Earthq Eng* 2012;40:34–47. doi:10.1016/j.soildyn.2012.04.002.
- 709 [42] Elsaid A, Seracino R. Rapid assessment of foundation scour using the dynamic features of
 710 bridge superstructure. *Constr Build Mater* 2014;50:42–9.
 711 doi:10.1016/j.conbuildmat.2013.08.079.
- 712 [43] Chopra AK. *Dynamics of Structures. A Primer*. Earthquake Engineering Research Institute;
 713 1981.
- 714 [44] Gutenbrunner G, Savov K, Wenzel H. Sensitivity Studies on Damping Estimation. Proc.
 715 Second Int. Conf. Exp. Vib. Anal. Civ. Eng. Struct., Porto, Portugal: 2007.
- 716 [45] Doherty P, Kirwan L, Gavin K, Igoe D, Tyrrell S, Ward D, et al. Soil Properties at the UCD
 717 Geotechnical Research Site at Blessington. Proc. Bridg. Concr. Res. Irel. Conf., Dublin,
 718 Ireland: 2012, p. 499–504.
- 719 [46] Gavin KG, Lehane BM. Base Load-Displacement Response of Piles in Sand. *Can Geotech J*
 720 2007;44:1053–63.
- 721 [47] Gavin KG, O’Kelly BC. Effect of friction fatigue on pile capacity in dense sand. *J Geotech*
 722 *Geoenvironmental Eng* 2007;133:63–71.
- 723 [48] Igoe D, Gavin K, O’Kelly B. The shaft capacity of pipe piles in sand. *J Geotech*
 724 *Geoenvironmental Eng* 2011;137:903–12.
- 725 [49] Gavin KG, Tolooiyan A. An Investigation of correlation factors linking footing resistance on
 726 sand with cone penetration results. *Comput Geotech* 2012;46:84–92.
- 727 [50] Gavin K, Adekunle A, O’Kelly B. A field investigation of vertical footing response on sand.
 728 Proc ICE, *Geotech Eng* 2009;162:257–67. doi:10.1680/geng.2009.I 62.5.257.
- 729 [51] PCB Piezotronics. Impulse Hammer 086D50. Model 086D50 Prod Specif 2018.
- 730 [52] Arany L, Bhattacharya S, Macdonald J, Hogan SJ. Design of monopiles for offshore wind
 731 turbines in 10 steps. *Soil Dyn Earthq Eng* 2017;92:126–52. doi:10.1016/j.soildyn.2016.09.024.
- 732 [53] Di Laora R, Rovithis E. Kinematic Bending of Fixed-Head Piles in Nonhomogeneous Soil. *J*
 733 *Geotech Geoenvironmental Eng* 2014:1–10. doi:10.1061/(ASCE)GT.1943-5606.0001270.
- 734 [54] Karatzia X, Mylonakis G. Discussion of “Kinematic Bending of Fixed-Head Piles in

- 735 Nonhomogeneous Soil” by Raeffaele Di laora and Emmanouil Rovithis. *J Geotech*
736 *Geoenvironmental Eng* 2016;142:04014126. doi:10.1061/(ASCE)GT.1943-5606.0001270.
- 737 [55] Goit CS, Saitoh M, Oikawa H, Kawakami H. Effects of soil nonlinearity on the active length
738 of piles embedded in cohesionless soil: Model studies. *Acta Geotech* 2014;9:455–67.
739 doi:10.1007/s11440-013-0257-0.
- 740 [56] Velez A, Gazetas G, Krishnan R. Lateral Dynamic Response of Constrained-Head Piles. *J*
741 *Geotech Eng* 1983;109:1063–81. doi:10.1061/(ASCE)0733-9410(1983)109:8(1063).
- 742 [57] Gazetas G, Dobry R. Horizontal Response of Piles in Layered Soils. *J Geotech Eng*
743 1984;110:20–40. doi:10.1061/(ASCE)0733-9410(1984)110:1(20).
- 744 [58] Randolph M. The response of flexible piles to lateral loading. *Geotechnique* 1981;31:247–59.
- 745